

Electronic Thesis and Dissertation Repository

4-17-2013 12:00 AM

Delta Relaxation Enhanced Magnetic Resonance - Development and Application of a Field-Cycling Contrast Mechanism

Yonathan Araya
The University of Western Ontario

Supervisor
Dr. Timothy Scholl
The University of Western Ontario

Graduate Program in Medical Biophysics
A thesis submitted in partial fulfillment of the requirements for the degree in Master of Science
© Yonathan Araya 2013

Follow this and additional works at: <https://ir.lib.uwo.ca/etd>



Part of the [Medical Biophysics Commons](#)

Recommended Citation

Araya, Yonathan, "Delta Relaxation Enhanced Magnetic Resonance - Development and Application of a Field-Cycling Contrast Mechanism" (2013). *Electronic Thesis and Dissertation Repository*. 1242.
<https://ir.lib.uwo.ca/etd/1242>

This Dissertation/Thesis is brought to you for free and open access by Scholarship@Western. It has been accepted for inclusion in Electronic Thesis and Dissertation Repository by an authorized administrator of Scholarship@Western. For more information, please contact wlsadmin@uwo.ca.

Delta Relaxation Enhanced Magnetic Resonance - Development and Application of a
Field-Cycling Contrast Mechanism

(Thesis format: Monograph)

by

Yonathan Tekle Araya

Faculty of Medicine & Dentistry
Graduate Program in Medical Biophysics

A thesis submitted in partial fulfillment
of the requirements for the degree of
Master of Science

The School of Graduate and Postdoctoral Studies
Western University
London, Ontario, Canada

© Yonathan Tekle Araya 2013

Abstract

Delta relaxation enhanced magnetic resonance (dreMR) is a novel imaging method capable of producing contrast proportional only to the concentration of the bound form of the targetable contrast agent using a dynamic field-cycling technique. The characteristic high relaxivity magnetic field dependence of bound paramagnetic contrast agents enables suppression of tissue contrast from unbound agents and unenhanced tissue, thereby increasing probe specificity. The dreMR technique requires an auxiliary actively shielded field-shifting insert electromagnet to modulate the strength of the main clinical magnetic field as a function of time during the relaxation and evolution periods of a pulse sequence.

Ablavar (approved for human use) binds specifically to serum albumin and has a strong magnetic field dependence for serum albumin around 1.5T. Native biological tissues and unbound Ablavar demonstrate very little magnetic field dependence. Using a custom dreMR preparatory pulse, where the strength of the B_0 field is modulated for different times, signal intensity from only the bound form of Ablavar can be produced.

This work entails further advancement of the dreMR method, where we investigate developing the dreMR contrast using phantoms loaded with and without Rabbit Serum Albumin and *in vivo* imaging using mouse subjects with prostate and breast cancer.

Keywords

Ablavar, dreMR, Delta Relaxation Enhanced MRI, Field-Cycled MRI, Magnetic Resonance Imaging, MRI Hardware, Insert Coil, Relaxation, Relaxivity, Serum Albumin, Targeted Contrast Agent.

Acknowledgments

I would like to acknowledge express my sincere gratitude to my supervisor Dr. Timothy Scholl for his guidance, support, encouragement, and patience. I am grateful for the new opportunities and experiences gained while working in his lab. With his directions, professional support, and assistance, Tim has provided me an invaluable education.

I would like to thank members of my advisory committee Dr. Blaine Chronik and Dr. Giles Santyr for their time, suggestions and helpful advice.

To my lab members Dr. Francisco Martinez and Patrick Lim, I am grateful and owe many thanks for all their help and involvement in my project. Thank you for the insightful discussions and assistance with the RF development, relaxometry measurements, dreMR phantom and *in vivo* imaging measurements. Thanks for the late nights you were both willing to stay for the long MRI scans it took to debug the equipment

To Dr. William Handler and Chad Harris, I am indebted for all the support, assistance, construction of the dreMR hardware and software development, and its integration with the MRI scanner. Thanks for your patience when it took forever and a day to get the tail vein catheter in the mouse needed for dreMR scanning. Thanks to Frank Van Sas and Brian Dalrymple for all their help, skills and ingenuity for all the one-of-a-kind dreMR equipment they produced.

I would also like to acknowledge the members of the 2nd floor Imaging Research Laboratories for their help throughout my masters with the nuances of the GE scanners including Trevor Szekeres, Adam Farag, Dr. Trevor Wade, and Dr. Alexei Ouriadov.

I am also grateful to Dr. Paula Foster and her lab members including Yuhua Chen, Vasiliki Economopoulos, Christiane Mallett, and Dr. Emiline Ribot for their assistance with the animal models. Thank you specifically to Dr. Ribot for her time and assistance with the mouse tail vein catheters for the dreMR *in vivo* imaging.

Finally, I wish to thank all my family for their love and support, words of encouragement, and commitment to persevere.

Table of Contents

Abstract.....	ii
Acknowledgments	iii
Table of Contents	v
List of Figures.....	vii
List of Tables	xi
List of Abbreviations.....	xii

Chapter 1 1

General Introduction.....	1
1.1 Magnetic Resonance Imaging.....	1
1.2 Principles of Magnetic Resonance Imaging.....	2
1.2.1 Signal.....	4
1.2.2 Relaxation Times	6
1.2.3 Longitudinal Relaxation Time, T_1	8
1.2.4 Transverse Relaxation Time, T_2	9
1.3 Contrast Agents.....	11
1.3.1 Relaxivity.....	12
1.3.2 Targeted Contrast Agents	15
1.3.3 Field Strength, B_0 , and Temperature Dependence	19
1.4 Field-Cycling Relaxometry.....	20
1.4.1 Field Cycling Magnetic Resonance Imaging.....	22
1.5 Thesis Objectives and Overview	24

Chapter 2..... 27

Construction, Design and Methods for dreMR Experiments	27
2.1 Improvements to dreMR B_0 Insert Coil and Hardware	28
2.1.1 dreMR B_0 Insert Coil	29
2.1.2 Gradient Amplifier and Control.....	32
2.1.3 Current Switch Box.....	33
2.1.4 Radiofrequency Coil.....	35
2.2 dreMR Integration with Scanner	36
2.2.1 Pulse Sequence.....	36
2.2.2 Preparatory pulse.....	38
2.3 Analysis of dreMR Contrast	39
2.4 Phantom Preparation	43
2.5 Field-Cycling Relaxometry.....	44
2.6 Animal Preparation.....	49
2.6.1 Prostate Cancer model.....	50
2.6.2 Breast Cancer model.....	50
2.7 Magnetic Resonance Acquisition and Image Processing	50
2.8 Magnetic Resonance Imaging.....	51
2.8.1 Phantoms.....	51
2.8.2 <i>In vivo</i> Research	52

2.8.2.1 Prostate Cancer Model	52
2.8.2.2 Breast Cancer Model.....	53
2.8.2.3 Healthy Mouse – DIR sequence	53
Chapter 3.....	55
Results	55
3.1 Relaxometry Data - Fitting Results Using Lauffer Model of Relaxivity	55
3.2 Phantom Images	58
3.2.1 dreMR Single Inversion subtraction.....	58
3.2.2 dreMR Double Inversion Recovery.....	60
3.3 <i>In vivo</i> Images	62
3.3.1 Prostate Cancer Model	62
3.3.2 Breast Cancer Model.....	64
3.3.3 Double Inversion Recovery.....	66
Chapter 4.....	68
Discussion.....	68
4.1 Discussion	68
4.2 Limitations and Future Work.....	72
4.2.1 Ablavar Binding and Relaxivity	72
4.2.2 Correlation with Histology and Visualizing Vascular Permeability	73
4.2.3 Imaging Technique Improvements	75
4.3 Conclusion	76
References	78
Appendix A - Permissions	82
Appendix B – Animal Protocol.....	83
Appendix C – Animal Protocol.....	84
Appendix D – CURRICULUM VITAE	85

List of Figures

Figure 1.1 Left: Magnetic moments of a spin population in the presence of an external magnetic field (B_0). Each magnetic moment precesses around the z -axis at the Larmor frequency. Right: The spins are aligned, producing a net magnetization parallel with B_0	3
Figure 1.2 Magnetic moment of a nuclide in the presence of an external magnetic field precessing along the axis of the applied field (z -axis) at the Larmor frequency (ω_0).....	4
Figure 1.3 Coherence of spins following a $90^\circ B_1$ RF pulse. Left: Boltzmann distributions of $N\uparrow$ and $N\downarrow$ spins in presence of magnetic field. Middle: Following an RF pulse, the net magnetization is flipped into the x - y plane and precesses at the Larmor frequency. Right: FID signal induced in an RF coil.....	6
Figure 1.4 Longitudinal (T_1) and Transverse (T_2) relaxation rate curves. (Adapted from McRobbie, DW. 2007).....	8
Figure 1.5 The Longitudinal Relaxation Experiment.....	9
Figure 1.6 The Transverse Relaxation Experiment.....	10
Figure 1.7 Parameters influencing relaxivity. (Adapted from Hermann, P <i>et al.</i> , 2008).....	14
Figure 1.8 The relaxation rates of various rat tissues, at 30°C , as a function of magnetic field strength. (Reprinted with permission: Koenig SH, Brown RD, 3rd, Adams D, Emerson D, Harrison CG. Magnetic field dependence of $1/T_1$ of protons in tissue. <i>Investigative Radiology</i> . 1984;19(2):76-81) (29).....	18
Figure 1.9 Typical field-cycling relaxometry pulse sequence (Adapted from Kimmich <i>et al.</i> , 2004). The recycle delay (zero field) has been omitted.....	21

Figure 2.1 dreMR insert coil. Top row: Left: Schematic drawing of the dreMR coil (provided by Dr. Scholl). Middle: Winding process of dreMR insert coil with wire straightening apparatus. Right: Misalignment of wire patterns (top) from original winding construction protocol, and example of measurement of wire positions after one winding layer of the primary coil (bottom). Bottom Row: dreMR coil on the patient bed inside MR scanner. The RF coil and water-heated mouse anaesthesia bed are placed in front of the dreMR coil to show their integration.....	31
Figure 2.2 dreMR gradient amplifier positioned next to MR scanner hardware in the scanner equipment room.....	33
Figure 2.3 The current switch box disconnects the dreMR from the gradient amplifier during image acquisition. The switch box switches to an auxiliary load when the dreMR insert coil is deactivated during image acquisition to remove any offset currents and noise. Right: Picture of the current switch box. Left: Schematic of the integration of the current switch box with the gradient amplifier, dreMR coil and bypass coil (Adapted from Alford., 2009).....	35
Figure 2.4 General dreMR pulse sequence diagram. LEFT: Single shift encode sequence. The ΔB field shifts support both positive and negative field shifts. RIGHT: The double field shift encode sequence (DIR).....	37
Figure 2.5 A detailed view of the preparation stage. P1, P2 and P3 times are graphically defined on the timeline.....	39
Figure 2.6 The arrangement of samples in the phantom. Samples from left to right contained increasing concentrations of RSA, ranging from 0 to 700 μM . Samples from top to bottom contained increasing concentrations of Ablavar, ranging from 0 to 1000 μM	44
Figure 2.7 Basic Nonpolarized and Prepolarized sequence. The upper trace shows the switching of field values between the fixed polarization field (B_p), the variable relaxation field (B_r), and the fixed detection field (B_d), whereas the bottom trace shows the RF pulse followed after a small delay by the FID acquisition.....	44
Figure 2.8 NMRD data was acquired using the Spinmaster FFC2000 1T C/DC (Stelar s.r.l., Italy) and MRIn equipment. NMRD data for magnetic field strengths ranging from 0.010 MHz to 42.49 MHz was acquired using the SpinMaster relaxometer (Top Left). Top Right and Bottom Row: The insertable field-cycling relaxometer system (MRIn, Stelar s.r.l., Italy) used to acquire NMRD curves for ± 0.25 T field shifts about the clinical field strengths of 1.5 T (Top Right and Bottom Row).....	47

Figure 3.1 Fitting Results Using Lauffer Model of Relaxivity for 80- μM sample of Ablavar measured at 37°C. The Lauffer model for inner-sphere dipole-dipole relaxation (red trace) has been fit to relaxivities derived from NMRD data at 37°C. (circles) Sample with 4% w/v Rabbit Serum Albumin. (triangles) No Rabbit Serum Albumin.

57

Figure 3.2 Phantom and MRI images. Top: Arrangement of the samples in the phantom. Samples from left to right contained increasing concentrations of RSA, ranging from 0 to 700 μM . Samples from top to bottom contained increasing concentrations of Ablavar, ranging from 0 to 1000 μM . Bottom: Subtraction of the T_1 -weighted images. Images A and B show the T_1 -weighted images using the dreMR pulse sequence with positive (A) and negative (B) field shifts of 0.221 T. Image C shows the resulting dreMR image using the dreMR subtraction method.....

59

Figure 3.3 Phantom and MRI images. Top: (A) Arrangement of the samples in the phantom. Samples from bottom to top contained increasing concentrations of RSA, ranging from 0 to 700 μM . Samples from left to right contained increasing concentrations of Ablavar, ranging from 0 to 1000 μM . (B) T_1 -weighted image using a standard fast gradient echo pulse sequence acquired at 1.5 T (no field shifting). (C) Image shows the resulting dreMR image acquired with the dreMR-DIR sequence. The dreMR-DIR method demonstrates the ability to both suppress and enhance signal intensities of various albumin concentrations bound to various Ablavar concentrations without any post processing.....

61

Figure 3.4 Axial image of a female NU/NU mouse under study that developed prostate cancer tumours on both flanks and imaged 28 days post PC-3M cell injections. Two 4-mm NMR vials containing 160 μM of Ablavar loaded (2) with and (1) without 4.0% w/v RSA were placed within the imaging region of the tumours to serve as dreMR contrast controls. Top: (A and B) T_1 -weighted images pre- and post-injection of Ablavar. (C) T_2 -weighted image indicating significant tumour volume. The tumours are demarcated and indicated with the arrows. Bottom (D and E). T_1 -weighted subtracted images of pre- and post-injection of Ablavar ((D) and (E)) indicate regions where gadolinium was present. (F) Resulting dreMR axial image using the dreMR subtraction method. Notice the dramatic change in contrast from the standard pre- and post-injection subtracted images compared to the dreMR image. The contrast from the dreMR image shows only signal intensities arising from the bound form of Ablavar and albumin.....

63

Figure 3.5 Axial and coronal images of a female NU/NU mouse under study that developed a large breast cancer tumour in the mammary fat pad and imaged 29 days post MDA-MB-231 cell injections. Two 4-mm NMR vials containing 160 μ M of Ablavar loaded (2) with and (1) without 4.0% w/v RSA were placed within the imaging region of the tumours to serve as dreMR contrast controls. Top: (A and B) T_1 -weighted images pre- and post-injection of albumin-targeted gadolinium contrast agent (Ablavar). (C) T_2 -weighted image indicating significant tumour volume. The tumours are demarcated and indicated with the arrows. Bottom (D and E). Resulting dreMR axial image using the dreMR subtraction method of (D) pre- and (E) post-injection of Ablavar. (F) T_1 -weighted post-injection coronal images with the tumour demarcated. (G) Resulting dreMR coronal image using the dreMR subtraction method post-injection of Ablavar. The dramatic change in contrast from the dreMR image shows only signal intensities arising from the bound form of Ablavar and albumin..... 65

Figure 3.6 Direct albumin imaging using the dreMR Double Inversion Recovery (DIR) pulse sequence. Two 4-mm NMR vials containing 160 μ M of Ablavar loaded with and without 4.0% w/v RSA were placed within the imaging region to serve as dreMR contrast controls. Top left (A): T_1 -weighted image using a standard fast gradient echo pulse sequence acquired at 1.5 T. Bottom left (B): dreMR-DIR image with 100 ms positive 0.221 T magnetic field shift (P2 Time) and 90 ms negative 0.221 T magnetic field shift. Right (C): Overlay of dreMR-DIR and T_1 -weighted image. The dreMR-DIR method enables suppression of unbound agents and unenhanced tissues contrast, thereby increasing agent specificity..... 67

List of Tables

Table 1. Longitudinal relaxation model using a modification of the Solomon-Bloembergen-Morgan theory formulated by R. Lauffer. The fitted parameters and their uncertainties (one standard deviation) are given in the following table.....	57
---	----

List of Abbreviations

B_0 field	Main magnetic field
DIR	Double Inversion Recovery
dreMR	Delta Relaxation Enhanced Magnetic Resonance
DTPA	Diethylene triamine pentaacetic acid
FDA	Food and Drug Administration
EMA	European Medicines Agency
Gd(III)	Gadolinium ion
HSA	Human Serum Albumin
Hz	Hertz
IGBT	Insulated Gate Bipolar Transistor
MRI	Magnetic Resonance Imaging
MR	Magnetic Resonance
MS-325	Gadofosveset trisodium or Ablavar
NMR	Nuclear Magnetic Resonance
NP	Nonpolarized
PBS	Phosphate Buffer Saline
r_1	Longitudinal Relaxivity
r_2	Transverse Relaxivity
RF	Radio frequency
ρ	Proton density
PP	Prepolarized
R_1	Longitudinal relaxation rate
R_2	Transverse relaxation rate
RSA	Rabbit Serum Albumin

SA	Serum Albumin
SNR	Signal-to-Noise Ratio
T_1	Longitudinal relaxation time
T_2	Transverse relaxation time
TE	Echo Time
TR	Repetition Time
w/v	Weight-to-volume ratio

Chapter 1

General Introduction

1.1 Magnetic Resonance Imaging

Magnetic Resonance Imaging (MRI) is a diagnostic imaging modality that has steadily evolved since the 1970's to provide unparalleled access to imaging of biological systems (1, 2). MRI is non-invasive, does not deliver ionizing radiation, and provides excellent spatial resolution. Its primary weakness is its low sensitivity and specificity, which can be improved with the use of contrast agents (1). MRI relies on the interaction of nuclear spin systems with an applied magnetic field (3). Applications and manipulation of various pulse sequences and magnetic field gradients provide anatomical images with superb soft tissue contrast. Modern MRI techniques not only allow for imaging of anatomy and pathology, but also the investigation of organ function and *in vivo* biochemistry.

This thesis entails the development and application of a novel magnetic resonance (MR) molecular imaging method called **delta relaxation enhanced Magnetic Resonance** (dreMR, pronounced “dreamer”) (4). Acting as both a device and method, dreMR uses field-cycling MR techniques in conjunction with clinical superconducting MRI systems to prepare image contrast related to the concentration of targeted contrast agents that have bound to their targeted molecules. The characteristic large magnetic field dependency of

relaxivity ($r_{1,2}$) of bound targeted paramagnetic contrast agents enables contrast suppression of unbound agents and unenhanced tissues contrast, thereby increasing the agents' specificity. The dreMR method requires additional specialized hardware to modulate the strength of the main clinical magnetic field to produce the dreMR contrast. An auxiliary, actively-shielded field-shifting insertable electromagnet is used to modulate the strength of the main clinical magnetic field as a function of time during the relaxation and evolution periods of a pulse sequence. The introductory chapter provides the necessary background for understanding both MRI and the dreMR principle and method, introducing MRI, field-cycling relaxometry, and field-cycling MRI concepts, as well as the principles of relaxation of MRI contrast agents and the potential to increase molecular specificity with magnetic field-cycling.

1.2 Principles of Magnetic Resonance Imaging

The basis of MRI relies on the interactions of nuclear spin systems with an external magnetic field. The dominant and most commonly observed nucleus in MRI is the proton of the water molecule, which possesses an intrinsic nuclear spin of $\frac{1}{2}$. Nuclear spin is a fundamental physical property which determines if the nuclei will be observable by MRI. The nuclear spin is comprised of the total sum of the individual contributions of both unpaired protons and neutrons, each exhibiting a $\frac{1}{2}$ -nuclear spin. Only nuclides that possess non-zero spin value are observable by MRI. The spin of any nuclide is proportional to its magnetic moment, μ ,

$$\mu = \gamma I \tag{1.1}$$

where γ is the gyromagnetic ratio and I is the spin quantum number. When the magnetic moment is placed in an external magnetic field, nuclei with non-zero spin will preferentially align themselves (to a small degree) with the magnetic field, represented by convention along the z -axis. When measured, (as in quantum mechanics) the magnetic moment will precess around the z -axis in one of two directions, parallel or antiparallel with the magnetic field. Within the bulk magnetization of the spins, a little more than half of the spins will preferentially align parallel with the external field, the lower energy state, producing a small net magnetization along the direction of the magnetic field, illustrated in Fig. 1.1. In the absence of a magnetic field, the magnetic moments of an ensemble of spins would be randomly distributed and produce a net magnetization of zero.

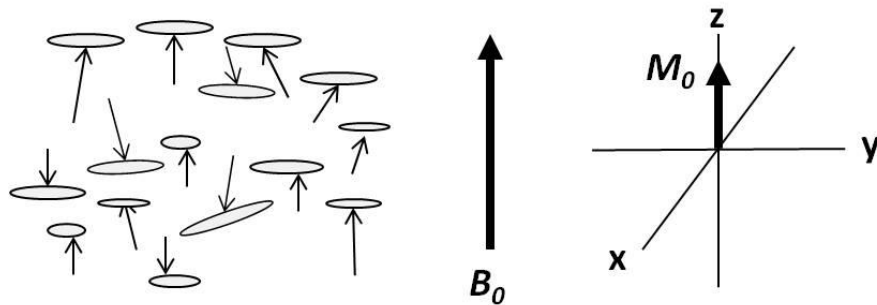


Figure 1.1 Left: Magnetic moments of a spin population in the presence of an external magnetic field (B_0). Each magnetic moment precesses around the z -axis at the Larmor frequency. Right: The spins are aligned, producing a net magnetization parallel with B_0 .

Within the bulk magnetization, while in the presence of an external magnetic field, individual nuclides will precess and resonate at a specific angular frequency, called the

Lamor frequency. The magnetic moment, μ , will precess around B_0 at the Lamor frequency, ω_0 , given by

$$\omega_0 = \gamma B_0 \quad (1.2)$$

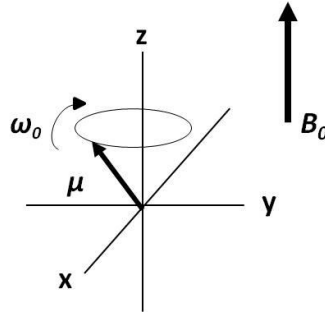


Figure 1.2 Magnetic moment of a nuclide in the presence of an external magnetic field precessing along the axis of the applied field (z -axis) at the Larmor frequency (ω_0).

MRI relies on the ability to manipulate the interaction of the bulk magnetization of spins with the external field produced by the superconducting MR magnet.

1.2.1 Signal

An MRI signal arises from the difference in energy absorbed or emitted during transitions between the two spatially oriented states. The energy of each state is given by \mathcal{E} , illustrated in Equation 1.3, where $I = \pm 1/2$, and thus the difference between the two states, $\Delta\mathcal{E}$, can be calculated from Equation 1.4. For the nuclide to transition to the higher energy state, N_{down} (anti-parallel), sufficient electromagnetic energy, $\Delta\mathcal{E}$, must be applied. Similarly, for the nuclide to transition to the lower energy state, N_{up} (parallel), sufficient electromagnetic energy, $\Delta\mathcal{E}$, must be emitted to conserve energy of the spin system. The ratios of the spin populations between the two orientation states, where N_{up} and N_{down} are

the spin population parallel and anti-parallel to the magnetic field respectively, can be calculated using the Boltzmann distribution (Equation 1.5),

$$\varepsilon = \gamma \hbar I B_0 \quad (1.3)$$

$$\Delta \varepsilon = \gamma \hbar B_0 \quad (1.4)$$

$$\frac{N_{up}}{N_{down}} = \exp\left(\frac{\Delta \varepsilon}{k_B T}\right) \quad (1.5)$$

where \hbar is Planck's constant divided by 2π , k_B is the Boltzmann constant, $1.3805 \times 10^{-23} \text{ J K}^{-1}$, and T is the temperature in Kelvin. The net magnetization, M_0 , is derived from the difference between the spin orientation states, illustrated in Equations 1.6 to 1.8.

$$N_{excess} = N_{up} - N_{down} = 1 + \frac{\gamma \hbar B_0}{k_B T} \text{ such that } \gamma \hbar B_0 \ll k_B T \text{ (through Taylor expansion)} \quad (1.6)$$

$$N_{excess} = \frac{N_{total}}{2} \cdot \frac{\gamma \hbar B_0}{k_B T} \quad (1.7)$$

$$M_0 = \frac{\rho \gamma^2 \hbar^2 B_0}{4 k_B T} \quad (1.8)$$

The ratio demonstrates that the net magnetization varies inversely with the temperature, and directly with the proton density (ρ), the gyromagnetic ratio, and the applied magnetic field.

In the bulk spin population, the individual spins will rotate at random phases around the z -axis when placed in a magnetic field. Coherence of the spins can be achieved when a 90° radio frequency (RF) pulse, B_1 , is applied at the Larmor frequency with a transmit RF coil. When the application of the RF pulse is applied for a sufficient

duration, the net magnetization will be flipped to precess at the same phase about the z -axis of the magnetic field in the x - y plane inducing a time varying magnetic field. From Faraday's law of induction, a voltage can be measured using an RF receiver coil sensitive to only the magnetization perpendicular to B_0 (in the x - y plane). The voltage signal detected by the receiver RF coil would be proportional to the amplitude of M_0 and precess at the Larmor frequency. The spins would precess about B_0 until the RF field is removed, thereupon the spin-relaxation processes would cause loss of coherence due to dephasing as magnetization returns to its equilibrium position parallel to the magnetic field. As the spins return to equilibrium (spin-lattice relaxation), the amplitude of M_0 would decay exponentially and produce a free induction decay (FID) signal, illustrated in Fig. 1.3.

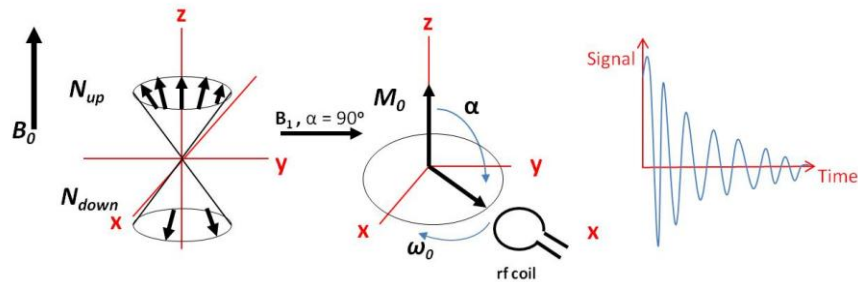


Figure 1.3 Coherence of spins following a $90^\circ B_1$ RF pulse. Left: Boltzmann distributions of N_{\uparrow} and N_{\downarrow} spins in presence of magnetic field. Middle: Following an RF pulse, the net magnetization is flipped into the x - y plane and precesses at the Larmor frequency. Right: FID signal induced in an RF coil.

1.2.2 Relaxation Times

Immediately after the excitation of the bulk magnetization, whereby sufficient RF energy is applied to convert the longitudinal magnetization to the transverse plane (x - y plane), relaxation mechanisms act on the spin system as it relaxes back to equilibrium.

The two predominant features of relaxation following the RF pulse include: the dephasing of the spins due to differences in their precessional frequencies and magnetic field inhomogeneities, and the regrowth and realignment to their equilibrium orientation along the z -axis parallel to the magnetic field. Following the loss of energy absorbed from the RF pulse, the longitudinal magnetization relaxes (spin-lattice relaxation) to the equilibrium orientation parallel to the z -axis of the magnetic field with a time constant T_1 . At the same time, the transverse magnetization decays exponentially and relaxes (spin-spin relaxation) with a time constant T_2 . The relaxation times vary with magnetic field strength and temperature. The difference between the time constants, T_1 and T_2 , are important for development of contrast in MR imaging. Biological tissues exhibit substantially different T_1 and T_2 values, and the additional administration of contrast agents can further enhance these values. Generally, tissues with short T_1 times yield greater signal intensity (brighter) than those with longer values due to a larger equilibrium magnetization (M_z), and tissues possessing short T_2 yield lower signal intensity (darker) due to a reduction in the detected transverse magnetization. The MR signal from an image is therefore dependent on the combination of the intrinsic tissue properties and extrinsic user-selected imaging parameters and contrast agents. The choice of specific pulse sequences with optimized parameters can be used to exploit tissues contrast and improve image quality.

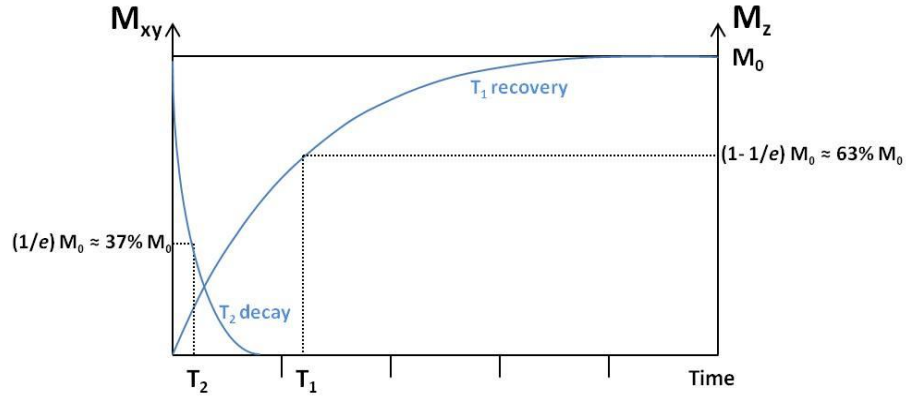


Figure 1.4 Longitudinal (T_1) and Transverse (T_2) relaxation rate curves. (Adapted from McRobbie, DW. 2007).

1.2.3 Longitudinal Relaxation Time, T_1

At equilibrium, the bulk magnetization produces a net magnetization, M_0 , parallel with the external magnetic field, B_0 . The longitudinal (T_1) relaxation, also known as spin-lattice relaxation, is described as the re-establishment of the equilibrium longitudinal magnetization M_z , along the z -axis following the application of a 90° RF pulse. The T_1 relaxation process, results in a loss of the absorbed RF energy to the spin system and the surrounding environment (lattice). The relaxation process emerges from the fluctuations in the local magnetic field due to the interactions between the spins and their environment as the molecule tumbles. The T_1 relaxation time is given by Equation 1.9, and is described as the time, τ , needed for z -component of the magnetization to recover to 63% of M_0 (Fig. 1.4).

$$M_z = M_0 (1 - e^{-\tau/T_1}) \quad (1.9)$$

T_1 times can be accurately measured by a simple NMR technique where sequential 90° RF pulses are applied with changing delay times, τ , in-between to examine

the M_z recovery (Fig. 1.5). Repeating the sequence for multiple delay times, the T_1 time can be determined by plotting the area under the FID versus τ , and fit with an exponentially decay function to extract the time constant T_1 (5).

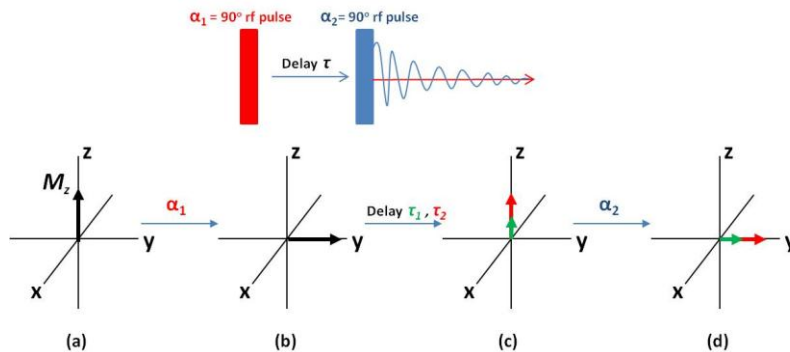


Figure 1.5 The Longitudinal Relaxation Experiment.

1.2.4 Transverse Relaxation Time, T_2

In the same time that T_1 relaxation occurs, where M_z recovers to equilibrium, the transverse magnetization, M_{xy} , decreases exponentially due to the dephasing of spins throughout the spin systems. The transverse (T_2) relaxation, also known as spin-spin relaxation, occurs following the application of a 90° RF pulse, where the spins dephase due to differences in their precessional frequencies. T_2^* relaxation occurs immediately following a 90° RF pulse, whereas T_2 relaxation occurs following 90° - 180° sequential RF pulses (also known as a spin echo sequence). The combined effects of the imperfections in the main magnetic field and the spin-spin interactions lead to the transverse magnetization decay. The relaxation process emerges from the molecular size and mobility of the tumbling molecules, where fast tumbling mobile molecules are able to average out the field inhomogeneities and intrinsic spin dephasing (leading to longer T_2 times), and large slow tumbling immobile molecules readily experience spin interactions

and field inhomogeneities (leading to shorter T_2 times) (2, 5). The T_2 relaxation time is given by Equation 1.10, and is described as the time needed to recover to 37% ($100 \times e^{-1}$) of M_0 (Fig. 1.4).

$$M_{xy} = M_0 e^{-\tau/T_2} \quad (1.10)$$

T_2 times can be accurately measured by a simple NMR technique where sequential 90° - 180° RF pulses are applied with changing delay times, τ , in-between to examine the M_{xy} decay (Fig. 1.6). The initial 90° RF pulse flips the net magnetization onto the transverse plane, where the spins begin to dephase at the Larmor frequency. The subsequent application of the 180° RF pulse refocuses the spins and forms an echo, allowing for detection of the FID signal. True T_2 decay however is determined from multiple 180° refocusing pulses, where the transverse signal will decay with the T_2 time constant and can be determined by plotting the data points from the decay curve (5). The single FID signal acquired from one 90° - 180° RF pulse decays with a T_2^* decay constant, which is dependent on the magnet and its field imperfections.

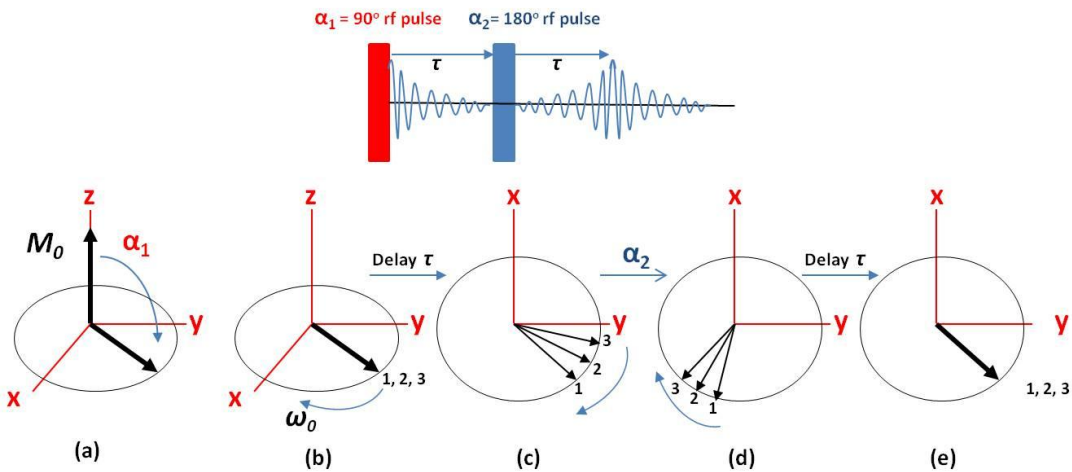


Figure 1.6 The Transverse Relaxation Experiment.

1.3 Contrast Agents

The contrast from MR images can be manipulated by changing the intrinsic biological tissues relaxation processes or the extrinsic user-selected pulse sequence parameters. The driving force for the use of contrast agents in MRI is to further enhance and/or differentiate signals arising from the biological tissues of interest. In the clinical practice, approximately 35% of all MRI examinations are performed with contrast agents (6, 7). Contrast agents are pharmaceutical drugs that directly affect the magnetic properties of water protons within their vicinity by increasing the protons' relaxation rates. Contrast agents are administered intravenously and exhibit properties such that they are highly soluble, well-tolerated, and chemically inert (chelated metal ions), and are rapidly eliminated from the body following the examination (8). The majority of contrast agents are chelates containing either Gd(III), Fe(III), Mn(II), or iron oxide ions (7-9). Paramagnetic (Gd(III), Fe(III), Mn(II)) contrast agents predominantly accelerate the T_1 relaxation process, resulting in positive signal enhancement, while superparamagnetic (iron oxide) contrast agents predominantly accelerate the T_2 relaxation process, resulting in negative signal enhancement (10). Gadolinium(III) is the most used and studied metal ion for use in MRI because of its seven unpaired electrons and ideal structural symmetry (8, 11). Due to the large molar concentrations required to allow for sufficient proton relaxation (10 -100 μ M) (9, 12), the metal ion complex must be chelated to reduce acute and chronic toxicity and increase *in vivo* stability and excretability (9). Recent developments have seen the ability to modify the chelating agent to increase target specificity by including selective binding biological vectors (7, 13).

In addition to the signal enhancement classification (T_1 vs T_2 action), all contrast agents can be divided based on their site of action: extracellular, organ-specific, or intravascular agents (10). Extracellular contrast agents distribute non-specifically throughout the plasma and interstitial space of the body (8), organ-specific contrast agents accumulate specifically in the targeted organ, and intravascular agents enhance the arterial and vascular structure for the period of the MRI exam (12). Historically, development of contrast agents have been focused on T_1 -based contrast agents, since the T_1 relaxation times are typically five times longer than T_2 and therefore easier to shorten (8, 10).

1.3.1 Relaxivity

The largest challenge in MR imaging is its relatively low sensitivity. As a result of the high concentration of commercial contrast agents (millimolar concentration) required to affect the relaxation rates of protons, there have been great efforts to increase the contrast sensitivity (8). The ability of a contrast agent to change the relaxation rate is characterized as its relaxivity, r_i . Relaxivity is defined as the efficiency with which the contrast agent enhances the proton relaxation rates (9).

$$r_i = \frac{R_{i,observed} - R_{i,buffer}}{[CA]} \quad i = 1,2 \quad (1.11)$$

where R_i is the inverse of the relaxation time, $\frac{1}{T_i}$, known as the relaxation rate, and $[CA]$ is the concentration of the contrast agent on a per Gd(III) basis. High relaxivity agents can be detected at lower doses and provide greater contrast at equivalent doses to current commercial agents with lower relaxivity (1, 8, 14). The two approaches to increasing the

relaxivity of contrast agents are to either increase the intrinsic molecular parameters that govern their relaxivity or to attach multiple metal (generally Gd(III)) ions within the complexes (1, 9). Attaching multiple metal complexes together to the molecular structure increases the agents' relaxivity by reducing the molecular tumbling, τ_r , due to an increase in molecular size. The interaction between the Gd(III) and the water molecules becomes more efficient by reducing the molecular tumbling, τ_r thereby increasing the effect on local relaxation rates (13). The intrinsic molecular parameters that govern relaxivity include hydration number, q , the distance between the Gd(III) ion and the water proton, the water exchange rate, the electronic relaxation time, T_{1e} , and the rotational correlation time, τ_c . (11, 15). Relaxation rates of water protons under the influence of Gd(III) are largely dominated by inner-sphere relaxivity, resulting from the dipolar contributions due to interactions with random fluctuations of the electronic field (15). The longitudinal relaxation arising from the inner-sphere relaxation can be modeled using a modified Solomon-Bloembergen-Morgan equation formulated by R. Lauffer (9) given by

$$r_1^{IS} = \frac{[M]}{[H_2O]} \frac{q_{IS}}{T_{1M} + \tau_m} \quad (1.11)$$

where $[M]$ is the molar concentration of the paramagnetic ion, $[H_2O]$ is the molar concentration of water, q_{IS} is the inner-sphere hydration number, T_{1M} is the relaxation time for bound inner-sphere water molecules and τ_m is the water residency time. Inner-sphere relaxation is inversely proportional to the metal-ion-proton distance to the 6th power. Achieving a reduced distance between the Gd(III) ion and bound protons in principle would increase relaxivity, since the inner-sphere relaxation is inversely

proportional to the metal-ion-proton distance to the 6th power. Reducing the metal-ion-proton distance would also allow for rapid exchange between the bound protons and the free water and efficiently distribute the relaxation effects (1, 11). All commercially approved Gd(III) contrast agents have one inner-sphere binding site, q_{IS} , for water protons. The ability to increase q_{IS} would increase relaxivity, as they are linearly proportional, however contrast agents that allow multiple binding sites for protons in their first coordination sphere experience reduced stability and increased concerns for toxicity (14). The rotational correlation time, τ_c , is largely dependent on the molecular tumbling correlation time, τ_r , the electronic relaxation time, T_{1e} , and the chemical exchange, τ_c . Field strength, molecular structure, and the biochemical environment dominate the efficiency of these time constants and contribute to the overall chemical exchange between the contrast agent, water proton, and bulk protons (1, 6, 14). Essentially, the contrast agent must be stable and chemically inert, allow for fast water exchange from the first coordination sphere, and efficiently relax the protons it contacts.

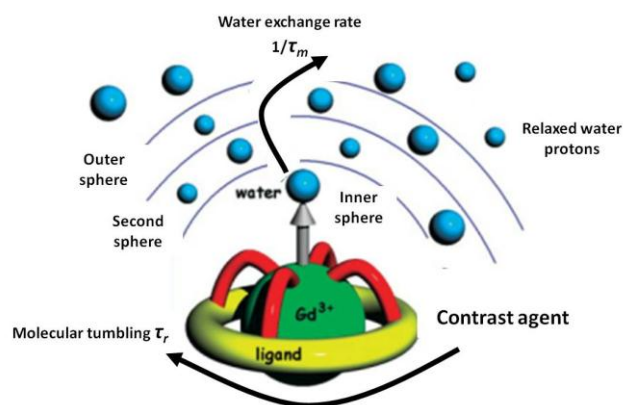


Figure 1.7 Parameters influencing relaxivity. (Adapted from Hermann, P *et al.*, 2008).

1.3.2 Targeted Contrast Agents

The development of targeted contrast agents involves optimizing both their affinity and specificity for its protein target (8). The challenge of synthesizing compounds with both high target affinity and relaxivity is an ongoing field of interest in medical chemistry (12). With the large micromolar doses required for sufficient contrast enhancement, current agents are limited to sites where accumulations of high concentrations are expected. Detection at the cellular and/or sub-cellular level would require nanomolar sensitivity, so that conventional Gd(III) agents are suitable (16). New generations of contrast agents are being developed to be site-specific and with increased tissue specificity, and as a result, higher relaxivities are required to compensate for the decrease in concentration needed to detect cellular and sub-cellular bioactivity (1, 6, 15-17).

Targeted contrast agents are defined by their mechanism of action, targeting either passively or actively. Passive targeting favours the specific distribution characteristics of tissues and cells and are generally either phagocytosed by macrophages or incorporated into components of the mononuclear phagocyte system (11, 13, 18). Active targeting selectively binds to molecular targets expressed within various diseases models including cell surface markers on immune cells or specific markers specifically expressed in certain stages of disease (11, 13, 18). Synthesizing compounds for targeted binding (through proteins, antibodies, or small peptides) improves relaxivity by slowing down the tumbling rate of the agent, thereby improving the agents' specificity. However the binding process is not always an effective strategy since binding to a large biomolecule can also alter the hydration number and water exchange rate within the inner-sphere (11) reducing the

inherent relaxivity of the agent. The challenges to maintain and/or improve the agents' relaxivity upon binding to their target biomolecule is evident by the limited number of contrast agents approved for clinical use with MRI by the Food and Drug Administration (FDA), European Medicines Agency (EMA), and Health Canada. In addition to the large target affinity, targeted contrast agents exhibit a strong relaxivity change in magnetic field dependence in both their targeted and non-targeted states (1, 6, 8-12, 14, 15, 17-21). Ablavar (Gadofosveset trisodium, (formerly known as MS-325 and Vasovist) Lantheus Medical Imaging, Inc. N. Billerica, MA, USA) binds to serum albumin and is the only current clinically available targeted MRI contrast agents available on the market. EP-2104R (EPIX Pharmaceuticals, Lexington, Massachusetts, USA) binds to fibrin (21), and is currently undergoing clinical phase trials. Ablavar differs from other polymeric Gd(III) complexes, most notably Albumin-GdDTPA. Albumin-GdDTPA, bound covalently to albumin, was a prototypical intravascular blood pool contrast agent that promised favorable contrast for vascular imaging; however, it was not approved for clinical use due to its poor stability, renal excretion rates, and low water solubility (7).

Albumin and fibrin are useful targeting moieties due to their micromolar concentrations, and specific pathological presence that can aid in specificity (19, 21). The most abundant protein in the blood plasma at concentration of 600-700 μM , albumin reversibly binds noncovalently with Ablavar to provide enhanced T_1 contrast (19). The reversible binding to albumin controls the leakage of the contrast agent to the intravascular space, allows for the nontargeted fraction to be filtered through excretion to the kidneys, protects the targeted fraction from filtration, and increases the agents' relaxivity approximately 10-fold at 20 MHz (for HSA) upon binding to the larger albumin molecule (67 kDa) (19, 20). Ablavar has moderate affinity for HSA, with reported

circulating concentrations of 0.1 mM, 88% of the administered Ablavar is noncovalently bound to HSA (19, 20), and *in vivo* studies have shown strong enhancement 1-hour post injection for animals and 24 hours for humans(19, 20). Originally used to measure liver function, nutritional status and diseases (Kawasaki, Pancreatitis) (22), recent evidence has shown albumin as a marker for angiogenic blood vessels presenting a major role in tumor microenvironment trafficking in and out of tumors, (23-26).

The high sensitivity and specificity of targeted contrast agents makes them advantageous for molecular imaging, however a major concern with regards to MRI not readily experienced in other imaging techniques (nuclear, optical), is the enhanced signal present from tissue in the vicinity of unbound agent and even signal from unenhanced background tissue (18). The issue is complicated by the high level of competing signal from all three instances (18). The signal arising from the unenhanced background tissue can be suppressed by scanning pre and post agent administration, however this of course requires two imaging scans and enough time for the agent to distribute and accumulate *in vivo*. Unfortunately, it becomes highly problematic when trying to distinguish targeted from non-targeted contrast agents since even with the high relaxivity enhancement in the targeted complex, the signals arising from both cases are indistinguishable. It is understandable that combining the advantages of MRI, which provides high-resolution anatomical images, with molecular sensitivity within a single imaging system would greatly aid and possibly simplify the process of detection of diseases. This was the basic premise of the dreMR: by exploiting the relaxivity magnetic field dependence possessed by only the bound form of the targeted agent, one could suppress both signal arising from the non-targeted contrast agent and unenhanced biological tissues, and only obtain signal arising from the targeted contrast agent (4, 27, 28). Novel relaxometry data published by

Koenig *et. al.* (Fig. 1.8), demonstrated the relaxation rate magnetic field dependence for six tissues in a rat.

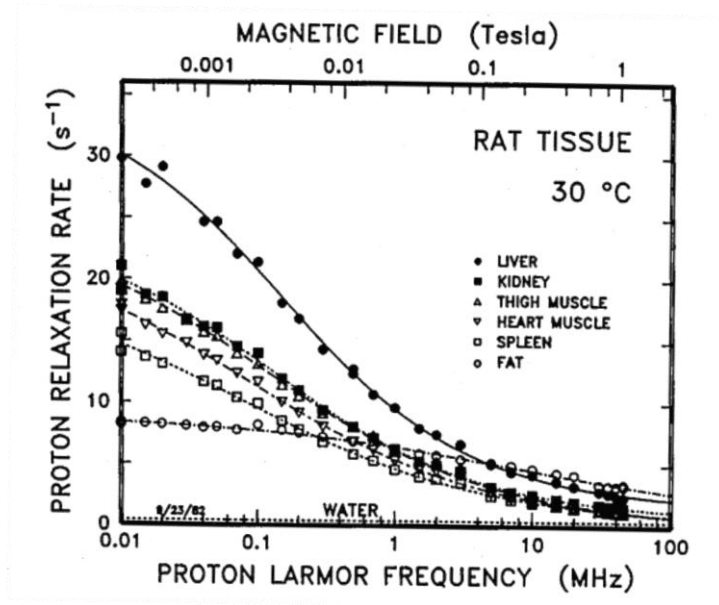


Figure 1.8 The relaxation rates of various rat tissues, at 30°C, as a function of magnetic field strength. (Reprinted with permission: Koenig SH, Brown RD, 3rd, Adams D, Emerson D, Harrison CG. Magnetic field dependence of $1/T_1$ of protons in tissue. *Investigative Radiology*. 1984;19(2):76-81) (29).

At lower magnetic field strengths, there is a large variation in the relaxation rate magnetic field dependence; however the relaxivities for all tissues begin to converge as the magnetic field strength increases above 0.1 T, minimizing the field dependence. A more important observation is that as the magnetic field strength approaches clinical field strength (>1 T), the change in R_1 , $\frac{\partial R_1}{\partial B}$, approaches zero for all tissues. Comparing the strong relaxivity magnetic field dependence of the targeted contrast with the minimal dependence of non-targeted contrast agents and unenhanced biological tissues, it becomes

apparent that signal arising only from the bound form of the targeted agent can be discriminated by modulating the magnetic field within a clinical MRI scanner.

1.3.3 Field Strength, B_0 , and Temperature Dependence

The relaxivity field dependence is an essential parameter to consider during the development and optimization of contrast agents, whether they are non-specific or targeted. Longitudinal and transverse relaxivities are strongly field dependent over limited ranges. As the applied magnetic field increases, the field dependence decreases for longitudinal relaxivity since the relaxation rates of the contrast agent and solvent converge (observation is reversed for transverse relaxivity) (1, 6, 14, 29). With the general trend towards higher fields in MRI, (3 T and beyond), to increase both sensitivity and resolution, the commensurate decrease in agent relaxivity reduces much of the potential gains (11, 29). An increase in field strength would also amount to an increase in tissue relaxation rates, suggesting contrast between normal and abnormal tissue will be field dependent as well (29). Water exchange rate, rotational diffusion, and correlation time, parameters governing relaxivity, are all temperature dependent, all increasing with temperature (1, 14, 17). It becomes necessary to understand the parameters governing both the relaxivity and relaxation times field dependence of the contrast agents and tissues to choose an optimal field for imaging, factors that impact whether the contrast agent will become clinically relevant (1, 6, 11, 14, 17, 29).

1.4 Field-Cycling Relaxometry

Conventional MRI uses a high-field superconducting magnet to both polarize and image (with the use of gradients systems and RF coils) the nuclei of an object, producing contrast from the relaxation properties (exploited by pulse sequences) of tissues. A field-cycling relaxometer directly measures the relaxation rates of samples by modulating the strength of the magnetic field during a series of magnetization evolution periods (30-32). The basic premise of field-cycling magnetic resonance is the ability to rapidly switch between magnetic strengths for relaxation and signal acquisition levels during the pulse sequence without causing artifacts or image degradation due to the fast switching for acquisition (30). Field-cycling of the magnetic field permits acquisition at one field strength so that a series of relaxation measurements at different field strengths can be obtained at a single acquisition field without re-tuning the NMR probe. The acquisition field is chosen predominantly to maximize signal strength.

As depicted in the general pulse sequence (Fig. 1.9), the sequence consists of three periods for which the magnetic field is switched and varied: the polarization (B_p), the relaxation (B_r), and the detection (B_d) fields. The initial polarization field serves to increase the Boltzmann nuclear magnetisation of the spin system, the relaxation field serves to allow the spin system evolve for a specified duration and relax, and finally the detection field serves to detect the resulting FID signal. An extended recycle delay is implemented to allow the resistive magnet system to rest before the next cycle, establishing a thermal equilibrium for magnet and power supply. Continuing the

sequence for a series of relaxation field strengths, one can generate a nuclear magnetic resonance dispersion curve for the relaxation times of the sample.

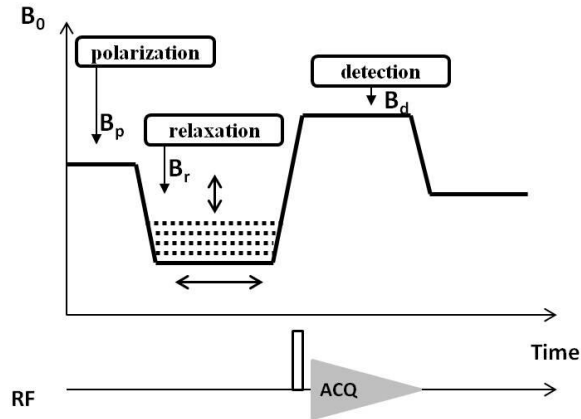


Figure 1.9 Typical field-cycling relaxometry pulse sequence (Adapted from Kimmich *et al.*, 2004). The recycle delay (zero field) has been omitted.

The preferred technique for field-cycling relaxometry consists of studying the field dependence of relaxation times (or rates). Studies employing the field-cycling technique have been regularly used to measure material properties, contrast agents and fluid interfaces, and biochemical interactions (32, 33). The evolution towards medical applications was predicated on the field dependence of normal and abnormal tissues, greatest at low field strength (< 0.4 T), ranging from $1 \mu\text{T}$ to 1.5 T (29, 31, 33-36). Relaxometry studies have shown field dependencies of various tissue diseased states, most notably of interest, Parkinson's and human brain cancers (29, 36-38). Applying field-cycling techniques to imaging would expand the ability to derive contrast from normal and abnormal tissues.

1.4.1 Field Cycling Magnetic Resonance Imaging

Conventional MRI is a multi-parameter imaging method that requires a stable, constant, homogenous magnetic field throughout the imaging process. Field-cycling MRI combines the techniques of field-cycling relaxometry with the imaging methods of MRI, offering access to biological information not available from conventional clinical imaging (39). Field-cycling MRI uses pulse sequences that differ from conventional MRI. During field-cycling MRI sequences, the magnetic field strength is modulated several times before signal detection by varying the current flowing through a resistive magnet that is inserted into the MRI bore or resistive-permanent magnet hybrid (33, 39). In this manner, the spin system evolves and relaxes at different relaxation fields to exploit the relaxivity field dependence, before returning to the scanner's usual field strength for signal detection. Field-cycling MRI alludes to measuring biophysical parameters by decoupling different contrast mechanisms (relaxation times) contributing to the MR signal (40-43). By exploiting the disparate magnetic field dependence of relaxivity for targeted contrast agents and unenhanced biological tissues with dreMR, new biophysical contrast parameters can be measured. Assessment of tumors, liver disease, and disorders of the brain, kidney, spleen, and pancreas would benefit from the quantitative measurements of field-cycling relaxometry and imaging (29, 32, 40, 42). The trade-off of field-cycling imaging over conventional MR imaging involves compromises such as increased imaging time, decreased spatial resolution and image quality regulated by reduced SNR. Implementation of this method has several technical challenges, which were investigated as part of this research. Interactions between the clinical and field-cycling magnet systems can lead to image artefacts resulting in misinterpretation of the biophysical

parameters (33, 34, 42). Careful construction of the field-cycling insert magnet including an accurately designed active magnetic shield and computer-controlled eddy current compensation has eliminated to a large extent almost all artefacts. With these technical challenges under control, this novel imaging contrast has been investigated to optimize various system and imaging parameters for comparison with conventional MR imaging.

1.5 Thesis Objectives and Overview

The work present in the thesis was completed by me in the Imaging Research Laboratories of the Robarts Research Institute under the supervision of Dr. Timothy Scholl as a Master's candidate in the Department of Medical Biophysics at Western University. This research involved a collaboration between the groups led by Dr. Scholl and Dr. Blaine Chronik in the Department of Physics and Astronomy at Western University. This included substantial assistance from Dr. Francisco Martínez-Santesteban (Scholl Group), Dr. William Handler (Chronik Group) and graduate student Mr. Chad Harris (Chronik Group). Many of the original ideas, which form the basis of dreMR were developed by Dr. Jamu Alford, a former Chronik graduate student and Dr. Brian Rutt (formerly at the Robarts Research Institute, presently at Stanford University). I also wish to acknowledge the input of Dr. Peter Caravan (Harvard University) who was the original developer of Ablavar and his research assistant, Dr. Christian Farrar, who have provided many helpful discussions. The overall goal of this project was to use Delta Relaxation Enhanced Magnetic Imaging to assess the albumin uptake in tumours in clinically relevant murine cancer models using the targeting MRI contrast agent Ablavar. Specific objectives included:

- 1) Use of field-cycling relaxometry techniques to measure and characterize the relaxivity of Ablavar
- 2) Application and integration of the new dreMR hardware and pulse sequence for dreMR imaging
- 3) Examination of Albavar-albumin binding using dreMR imaging to distinguish only the targeted form of the contrast agent.

Chapter 2 discusses the development and application of the field-cycling relaxometry techniques to measure the relaxivity of Ablavar, the implementation of the new dreMR hardware, pulse sequences, and the integration with the clinical MRI scanner. Chapter 3 presents the experimental findings and the resulting dreMR images from the single inversion and double inversion pulse sequence using both phantoms and *in vivo* murine cancer models. Chapter 4 summarizes the key experimental findings and the significance and implications of dreMR imaging. Current limitations and future directions to improve dreMR imaging are also discussed.

The samples for Ablavar-albumin relaxation rates measurements were prepared by me. Their measurements and relaxivity data analysis were completed by me and Dr. Martínez-Santesteban, with guidance from Dr. Scholl. The relaxivity modeling using the Lauffer Model of Relaxivity was provided by Dr. Scholl. Dr. Alford and Mr. Chad Harris provided the electromagnetic simulation models for the dreMR insert coil and the active shield. The construction of the dreMR insert coil was completed by Mr. Frank Van Sas and Mr. Brian Dalrymple under the supervision of Drs. Scholl and Handler. Mr. Harris and I provided assistance during the construction process. The National Instruments control software was provided by Dr. Handler. The modified Triple Inversion Recovery MRI pulse sequence was provided by Dr. Jeff Stainsby (GE Healthcare). The solid state switch box was previously built by Dr. Alford and Mr. Doug Hie (Physics and Astronomy Electronics Shop). The gradient amplifier was installed and matched to the dreMR coil by Joseph Venditto (Performance Controls Incorporated). I built the RF birdcage coil with assistance and feedback from Patrick Lim. The breast and prostate cancer models were provided by Dr. Paula Foster and her students Ms. Vasiliki Economopoulos and Ms.

Christiane Mallett. I was responsible for animal preparations during the *in vivo* dreMR studies, with assistance from Dr. Emeline Ribot for the mouse tail-vein catheter. The water heated mouse anaesthesia bed was designed by Dr. Scholl, and built by Misters Van Sas and Dalrymple. Drs. Scholl, Handler, Martínez-Santesteban, Mr. Harris, and I participated in the imaging sessions and image analysis. The phantom and *in vivo* dreMR images were processed and analyzed by me. Finally, Dr. Scholl, as principal author's supervisor, provided guidance and mentorship, helped determine the overall thesis objectives, reviewed project results, and provided editorial assistance with the thesis manuscript.

Chapter 2

Construction, Design and Methods for dreMR Experiments

The ability to prepare and derive image contrast related to the concentration of only the bound targeted contrast agent requires additional specialized hardware that must be added to a clinical superconducting MRI system. For ordinary magnetic resonance imaging, contrast enhancement is achieved using pulse sequence parameters and contrast agents that take advantage of the relaxation properties of the tissues of interest. This process unfortunately suffers from competing signal arising from unenhanced tissues and enhanced tissue from the contrast agent in its targeted and non-targeted states. To identify the image contrast from only the targeted agent, one would be required to scan pre and post contrast agent administration. This method does not discriminate between tissues enhanced by bound or unbound contrast agent; however with dreMR imaging, contrast agents bound to their target can be directly imaged eliminating the need for baseline imaging. dreMR imaging uses field-cycling MR techniques to modulate the strength of the main clinical magnetic field to produce the contrast enhancement only from the targeted form of the contrast agent. The dreMR method can be simply described as a actively shielded B_0 insert coil within an unmodified clinical superconducting MR system, controlled by additional supportive hardware and software to prepare sample magnetization for standard MR imaging. For this purpose, a redesigned 2nd-generation

dreMR coil was constructed specifically for small animal imaging (mouse-sized), to include improvements in mechanical, electrical and thermal design (44, 45).

Chapter 2 forms the basis of the design, construction and hardware improvements to the dreMR insert coil and the supplemental hardware and software. The fundamentals of the dreMR coil are described, as well as the required hardware and software sequences to perform dreMR imaging. The supplemental hardware and software include the fast current switch box to isolate the dreMR coil from the MR scanner during image acquisition, the power amplifier to drive the dreMR coil, the control systems hardware and software for integration and synchronization with the MR scanner, the RF coil, and the modified Triple Inversion pulse sequence with the dreMR magnetic field shifting preparation stages. All of the equipment was tested offline (outside the MR scanner room) before integration with the scanner to insure proper operation and to protect personnel and equipment. Preparations for the phantom and animal models are discussed, as well as the MRI acquisition and the image processing required to produce the dreMR images. The field-cycling relaxometry measurements and preparations of the Albavar-albumin concentrations is presented, including the Lauffer Model of Relaxivity, to demonstrate how the dreMR contrast is derived from the relaxivity magnetic field dependence of the Albavar-albumin complex.

2.1 Improvements to dreMR B_0 Insert Coil and Hardware

In its fundamental form, the dreMR insert coil must produce nearly uniform field shifts (> 0.1 T) within milliseconds without disrupting the stability of the host scanner and withstand the potential torques and forces as a result of Lorentz forces. To produce the desired uniform magnetic field shifts and minimize coupling interactions with the host

MRI scanner, the auxiliary insert coil needed to observe specific design criteria, specifically force and torque balancing, magnetic field homogeneity, inductance and ramping timings, heat dissipation through efficient cooling, and perhaps most importantly, magnetic coupling with the host MRI scanner.

2.1.1 dreMR B₀ Insert Coil

The dreMR insert coil is not directly involved in the process of imaging the sample, but rather acts to specially prepare sample magnetization before imaging with the host MRI scanner. The dreMR insert coil produces magnetic field shifts for tissue magnetization and then is turned off during signal acquisition. As a result, the homogeneity requirement for dreMR is much less than for the clinical magnet. Field calculations based on the electromagnetic designs indicate that inhomogeneity over a 20-mm-diameter, 40-mm-long-cylinder is 1.5% (approximate imaging volume of a mouse). This limited inhomogeneity has only a very limited affect on dreMR contrast producing an unnoticeable shading.

The requirement to repetitively ramp the magnetic field (on the order of milliseconds) on and off has the potential to produce eddy-currents capable of inducing instabilities in the main field that persist throughout signal acquisition, most notably phase and slice select artefacts. The dreMR insert coil was composed of two concentric electromagnets, a small solenoid primary coil for producing the magnetic field shifts and a counter-wound shield coil to largely eliminate the insert's fringe fields and coupling with the host MRI scanner.

Previous design calculations, methods, materials, and constructions techniques have been described (44, 46, 47); however, efforts have been made to improve the construction of the active shield for this newest device (45). There were inherent practical errors related to methods of construction and winding for the first-generation dreMR insert coil, such that the final constructed coil deviated from the original theoretical design. For example, subtle twisting of the magnet windings for the primary solenoid causing positional variations in both the longitudinal and radial wire locations compared with the ideal electrical design. This, in turn led to an accumulation of these small variances eventually causing a net misplacement of the entire coil on the former bobbin. The construction protocol was adapted to minimize the inherent winding errors and create a more realistic model of the primary coil. During winding, a wire “straightener” was used to remove small bends from the square hollow copper wire (5-mm width, 3-mm hole diameter) prior to winding onto a cylindrical G-10 former to create the primary coil (6 radial layers, 30 wire turns per layer, 15 turns per half, inner diameter of 8 cm, and length of 17 cm) (45). In addition, the actual positions of each individual wire loop were measured at each solenoid layer and used in a final design of the active shield. (45). The resulting single-layer shield wire pattern was counter-wound onto a second cylindrical G-10 former with diameter and total length of 28.8 cm and 30.5 cm respectively.

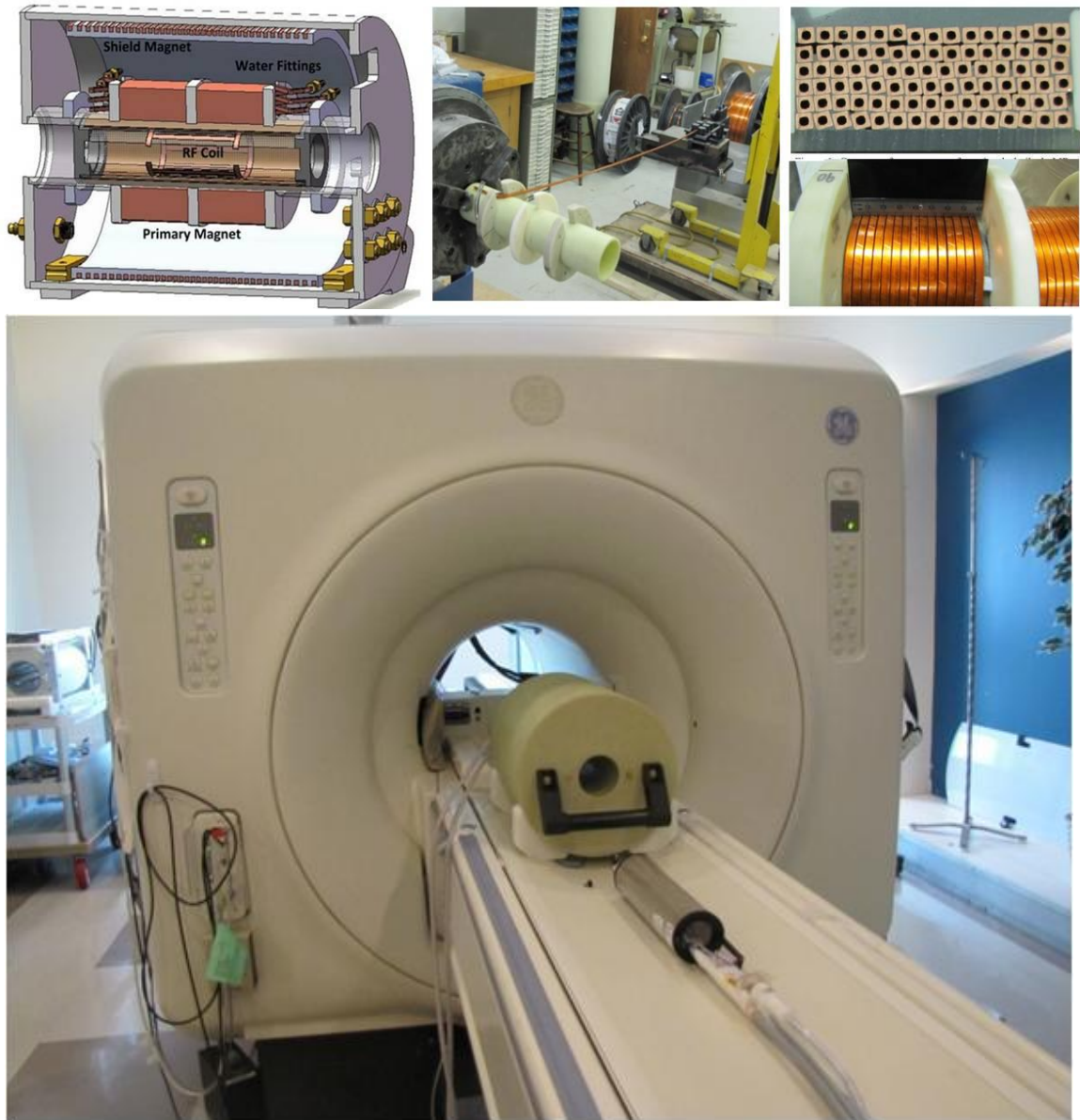


Figure 2.1 dreMR insert coil. Top row: Left: Schematic drawing of the dreMR coil (provided by Dr. Scholl). Middle: Winding process of dreMR insert coil with wire straightening apparatus. Right: Misalignment of wire patterns (top) from original winding construction protocol, and example of measurement of wire positions after one winding layer of the primary coil (bottom). Bottom Row: dreMR coil on the patient bed inside MR scanner. The RF coil and water-heated mouse anaesthesia bed are placed in front of the dreMR coil to show their integration.

Estimates of improved shielding due to the inclusion of measured wire positions for accurate calculation of the active shield geometry suggest gains in shield effectiveness

of better than 15%. Specifications for the second-generation dreMR B_0 insert coil, designed for mouse imaging include a cylindrical imaging region approximately 5-cm long and 2.5-cm in diameter. Physical parameters are: 42-cm length, 8-cm inner diameter, 32-cm outer diameter and 50-kg mass. Electrical parameters include 1.46-mH inductance, 96.4-m Ω resistance and 0.8697-mT/A magnetic field efficiency (44, 45).

2.1.2 Gradient Amplifier and Control

The shielded dreMR B_0 insert coil was powered by a QDCM 700 series gradient amplifier (Performance Control Inc., PA, USA). The internal feedback circuit of the gradient amplifier was calibrated to match the inductance (1.46 mH) and resistance (96.4 m Ω) of the dreMR insert coil, ensuring the gradient amplifiers faithfully reproduced the input waveforms generated by the National Instruments control hardware (NI DAQ). The NI DAQ was controlled by custom software written in LabView (National Instruments, version 11.0) running on a separate laptop computer. Waveform synchronization between the NI DAQ and the MRI console was realized by means of a transistor-transistor logic (TTL) trigger generated by the MRI system electronics initiated by the modified pulse sequence. The gradient amplifier and NI DAQ were housed in the MRI electronics equipment room, and communication between the NI laptop software and NI DAQ were performed via a 20-m long unshielded fiber-optic Universal Serial Bus (USB) cable to limit potential electromagnetic noise.

Notable specifications for the bipolar dual-axis gradient amplifier included peak output current of 430 A for 20 ms, peak output voltage 725 V, output current 270 A rms over a 300-s averaging window, 200 A rms for greater than 300 s, and a risetime to

maximum current of 300 μ s. From these specifications, it was possible to reliably achieve a maximum constant magnetic field shift of 375 mT over a 300 s scan and maximum slew rate of 400 T/s with the dreMR B_0 coil.



Figure 2.2 dreMR gradient amplifier positioned next to MR scanner hardware in the scanner equipment room.

2.1.3 Current Switch Box

The dreMR field homogeneity ($\sim 1.5\%$) is modest compared to that of the host scanner. This is not a limitation since the field is nominally zero during the image acquisition. However, small current offsets or fluctuations from the gradient amplifier powering the dreMR magnet can cause significant image artefacts due to the high field efficiency of the magnet system (0.8697 mT/A). A switch is therefore required to disconnect the dreMR from the gradient amplifier during image acquisition. The gradient

amplifier is designed to drive inductive loads. Its control circuitry supplies a current through the load that is proportional to an input voltage. Even when the input voltage is nominally zero, small offsets present anywhere along the input chain or in the amplifier circuitry are sensed and converted to a small output current. In the absence of a connected load, this will drive the amplifier outputs to maximum voltage. An auxiliary load with an inductance that is similar to that of the dreMR electromagnet to prevent current feedback oscillations must be substituted when the dreMR insert coil is isolated from the current source. A solid-state fast switch box was used to switch to an auxiliary “dummy load” (an inductor and power resistor in series chosen to match the electrical characteristics of the dreMR electromagnet, labeled bypass coil in Fig. 2.4) when the dreMR insert coil was deactivated during image acquisition. Design and construction of the fast switch box had previously been described (4) such that either the dreMR insert or the dummy load was attached to the amplifier at all times to prevent runaway current oscillations from damaging the amplifier. The switch box circuit contained two custom-built solid-state sub-switches, each with two 400-A 1200-V insulated gate bipolar transistors (IGBT) (POWEREX 400HA-24A), biased with an optically-isolated driver circuit (POWEREX BG2A-NF), and two 300-A 1200-V diodes (POWEREX CS641230). Bipolar current waveforms were achievable with the two separate IGBT current pathways. The high-current diodes prevented reverse current from overloading the protection diode in the transistors while in their off non-conducting state. Product specifications for IGBT and diode specified a continuous maximum peak current was 300 A with a 800-ns switching time for the diode, and a maximum peak current was 800 A with a 600-ns time for the IGBT. The fast switch box circuitry and dummy solenoid load were mounted on a 19-inch-wide 1000-W fan-cooled heat sink (TW7-1275-flsx, D6

Industries, Massachusetts, USA) to prevent overheating. Temporal control of the fast switching circuitry was achieved with TTL signals from the NI DAQ hardware synchronized to the pulse sequence.

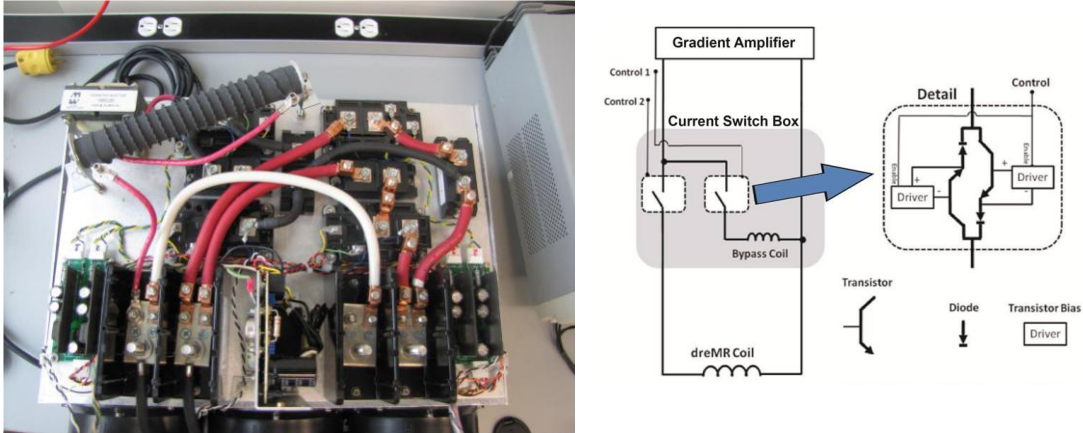


Figure 2.3 The current switch box disconnects the dreMR from the gradient amplifier during image acquisition. The switch box switches to an auxiliary load when the dreMR insert coil is deactivated during image acquisition to remove any offset currents and noise. Right: Picture of the current switch box. Left: Schematic of the integration of the current switch box with the gradient amplifier, dreMR coil and bypass coil (Adapted from Alford., 2009).

2.1.4 Radiofrequency Coil

A custom highpass, capacitively-matched, cylindrical eight-rung birdcage RF coil was built for the second-generation dreMR insert coil. The RF coil was to be tuned to the proton Larmor frequency at 1.5 T (63.86 MHz) with an imaging volume of 5 cm. The RF coil was shielded with a 150- μ m stainless steel mesh cylindrical shield to reduce noise and coupling with the dreMR insert coil. The RF coil was securely attached with an extended arm screwed into the exterior of the dreMR insert coil to prevent RF coil movement during the magnetic field shifting produced by the dreMR insert coil. The same RF coil was used throughout all phantom and *in vivo* imaging sessions.

2.2 dreMR Integration with Scanner

The dreMR imaging method requires custom software to implement the field shifting required to exploit the relaxivity field dependence of the targeted contrast agents and tissues. The dreMR pulse sequence consists of two parts: a preparatory stage, and an imaging stage. The dreMR insert coil was activated during the preparatory stage to provide the required field shift for magnetization of the spin systems and then deactivated during the imaging stage. Precise synchronization of the dreMR insert coil and MRI console was an integral component to acquire meaningful contrast and images that were free of artefacts. The dreMR insert coil was controlled by a NI DAQ system executing custom software in LabView (National Instruments Corp. USA) by a separate laptop computer in the MRI console station. The custom software is summarized in section 2.2.1. Synchronization was achieved by a TTL trigger generated by the MRI system electronics during the pulse sequence.

2.2.1 Pulse Sequence

The dreMR pulse sequence was based on a standard imaging sequence known as the Triple Inversion Recovery, controlled by the Blood Suppression imaging option, on a GE Healthcare 1.5 T CVMR scanner (WI, USA). The Triple Inversion Recovery pulse sequence contains user-specified delays between the 90° and 180° RF pulses for fat-water-blood suppression. The RF timing delays were leveraged to insert the preparatory stage required for the dreMR field shifting of B_0 , which under normal imaging situations would be held at the native field strength of the scanner. In total, the dreMR pulse sequence contained the preparatory stage required for the dreMR field shifting (including TTL output signals for hardware synchronization) followed by an imaging stage for

acquisition. The imaging sequence used was a Fast Spin Echo XL (FSE-XL). The preparatory sequence is identical to what is played out in double/triple IR-prepared FSE scans for black blood imaging of the heart. The preparation stage included options such that the RF pulses could be suppressed when not required and the time duration of the field-shifting portion could be optimized. The preparation stage was capable of including either one or two dreMR field shifts that could be separately specified for pulse duration and amplitude. The dreMR pulse sequence is generalized in figure 2.2. The simplest implementation of the dreMR pulse sequence included application of a 90° RF pulse, followed by a single dreMR field shift (either negative or positive) and then standard image acquisition (designated: 90° -[Field Shift]-[Acquire]). The single field shift encode also supported a 90° - 180° -[Field Shift]-[Acquire] scheme. A new double field shift encode, also known as the dreMR double inversion recovery (4), was developed using a 90° - 180° -[positive Field Shift]- 180° -[negative Field Shift]-[Acquire] scheme, integrating both the positive and negative field shifts as part of the same preparation phase of the pulse sequence. The first 90° pulse in the preparatory stage is a hard pulse, whereas the 180° RF pulses are adiabatic.

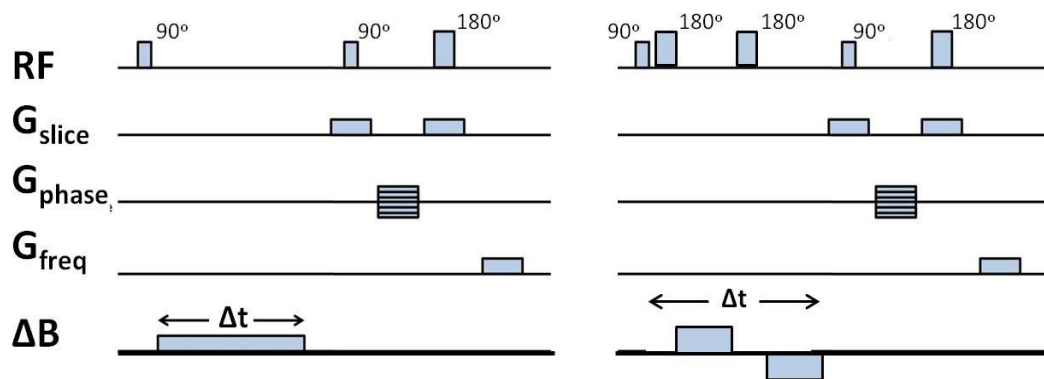


Figure 2.4 General dreMR pulse sequence diagram. LEFT: Single shift encode sequence. The ΔB field shifts support both positive and negative field shifts. RIGHT: The double field shift encode sequence (DIR).

2.2.2 Preparatory pulse

The preparatory stage of the dreMR sequence contains a number of necessary sequence parameters to completely specify either a single or double field shift encode. Different parameters are either activated or suppressed to achieve the desired preparatory sequence. The sequence provides user control for the time durations between the 90° - 180° RF pulses, the 180° - 180° RF pulses, the 90° (or 180°) RF pulse to image acquisition, the time durations of the field shifts, and tunable delays between the RF pulses and field shifts. The dreMR preparatory stage (Fig 2.5) is reduced to six important variables: the P1 time, the P2 time, the P3 time, the delay before the TTL turns on, and the positive and negative field shift durations. These parameters correspond to the times indicated on figure 2.3. The parameters are paramount to ensuring that not only does the preparatory stage provide the desired field shift, but that there are no timing overlaps between the preparatory stage and imaging stage. For clarification, the P1 time is the time from the start of the first RF pulse to the middle of the second RF pulse, P2 time is the time from the middle of the second RF pulse to the middle of the third RF pulse, and the P3 time is the time from the middle of the third RF pulse to the start of normal FSE acquisition.

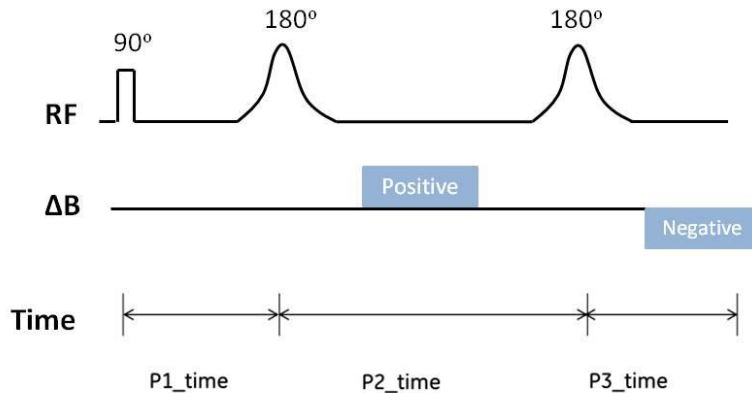


Figure 2.5 A detailed view of the preparation stage. P1, P2 and P3 times are graphically defined on the timeline.

To achieve a single encode field shift dreMR pulse sequence, both the 180° RF inversion pulses and P3 time are suppressed such that the preparatory stage only consists of the P1 and P2 time durations with a positive or negative field shift (90° -[Field Shift]-[Acquire]).

To achieve a double shift encode field shift dreMR pulse sequence, the entire preparatory sequence would be played out (Fig. 2.5).

2.3 Analysis of dreMR Contrast

Contrast derived from dreMR imaging, colloquially referred to as dreMR contrast, produces biophysical information not readily present with standard MRI techniques. dreMR imaging produces image contrast related to the magnetic field dependence of relaxation for a biological sample. The contrast is obtained due to the relative lack of relaxation rate, R_1 , field dependence from unenhanced tissues and tissues enhanced by non-targeted contrast agents (29, 32, 40, 48). Taking advantage of the intrinsic lack of T_1 dispersion of the unenhanced tissues and non-targeted contrast agents, dreMR imaging produces contrast arising only from signal enhancement of tissues by only the bound form

of targeted contrast agents (4, 28, 49). The relaxivity magnetic field dependence of the targeted form of contrast agent is measureable by manipulating the magnetic field strength of the MRI system during the preparatory stage of the pulse sequence prior to signal acquisition. It is therefore the change in R_1 with respect to the magnetic field strength, $\partial R_1/\partial B_0$, that is important for dreMR contrast (Equations 2.1-2.4). Given that

$$R_{1,enhanced} = R_{1,unenhanced} + r_1 \cdot [CA] \quad (2.1)$$

the partial derivative of $R_{1,enhanced}$ with respect to the magnetic field, B_0 is simply

$$\frac{\partial R_{1,enhanced}}{\partial B_0} = \frac{\partial R_{1,unenhanced}}{\partial B_0} + \frac{\partial r_1}{\partial B_0} \cdot [CA] \quad (2.2)$$

This relationship can be further simplified by the observation that

$$\frac{\partial R_{1,unenhanced}}{\partial B_0} \approx 0 \text{ (for } B_0 > 1.0 \text{ T)} \quad (2.3)$$

an approximation that is supported by literature (1, 8-10, 14, 29, 31, 48) and results acquired from field-cycling relaxometry data. This results in a very simple relationship relating the change in R_1 with respect to the magnetic field strength, contrast agent concentration and the magnetic field dependence of contrast agent relaxivity:

$$\frac{\partial R_{1,enhanced}}{\partial B_0} \approx \frac{\partial r_1}{\partial B_0} \cdot [CA] \quad (2.4)$$

There are two approaches to producing dreMR contrast. The simplest method involves the weighted subtraction of two T_1 -weighted images with different dreMR magnetic field shifts, one with a positive (T_{1+}) and the other with a negative (T_{1-}) magnetic field shift during the preparatory stage of the pulse sequence (27). Subtraction

of the T_{1+} and T_{1-} images would produce an image where the intensity would be due to the magnetic field dependence of the biological tissues and administered targeted contrast agent.

A simplified derivation of the dreMR subtraction method is summarized below. The derivation assumes the pulse sequence starts with a saturation radiofrequency pulse to eliminate pre-existing longitudinal magnetization followed by a ΔB preparatory pulse. The effect of finite ramping times for the ΔB preparation pulse (i.e. effective offset field, ΔB_{eff}) is ignored since the ramping times ($\sim 1-2$ ms) are significantly less than the duration of the pulse (~ 300 ms). Application of the field-shifting pulse has two effects, it modulates the steady state longitudinal magnetization and it changes the relaxation rate, R_1 of the sample. The steady-state longitudinal magnetization is proportional to the amplitude of the sum of the field-shifting and clinical magnetic fields. The application of a ΔB preparation pulse scales M_0 (the longitudinal magnetization at the clinical field strength) by a factor of $(B_0 \pm \Delta B)/B_0$, effectively increasing the magnetization for a positive preparatory pulse and decreasing it for the negative preparatory pulse. The longitudinal magnetization, $M_{z\pm}$, available for imaging after a preparatory pulse $\pm\Delta B$ of duration, Δt , is therefore

$$M_{z\pm} = M_0 \cdot \frac{B_0 \pm \Delta B}{B_0} \cdot [1 - \exp(-\Delta t \cdot R_{1\pm})] \quad (2.5)$$

where $R_{1\pm}$ is the relaxation rate for the sample at a magnetic field strength of $B_0 \pm \Delta B$.

The resulting image intensity of a positive or negative magnetic dreMR field shift is determined by extrinsic MR hardware, software and the readout sequence. A scaling factor, k , can be included to account for the intrinsic and extrinsic factors (proton density,

radiofrequency coil homogeneity, transverse relaxation time, etc.), therefore the final image intensity would be the product of the scaling factor and M_z

$$I(x, y, z) = k(x, y, z) \cdot M_z(z) \quad (2.7)$$

The dreMR subtraction methods takes the normalized difference of field-shifted images, I_+ and I_- . This normalization removes the influences of the changing equilibrium magnetization described above.

$$I_{Sub} = \left| I_- \frac{B_0}{B_0 - \Delta B} - I_+ \frac{B_0}{B_0 + \Delta B} \right| \quad (2.8)$$

$$I_{Sub} \approx k M_0 \cdot [(1 - \exp(-\Delta t \cdot R_{1-})) - (1 - \exp(-\Delta t \cdot R_{1+}))] \quad (2.9)$$

If the assumption is made that $\partial R_1 / \partial B_0$ is constant in the vicinity B_0 , it is possible to approximate $R_{1\pm} = R_1 \pm \Delta R_1$ for the resulting image intensity. This assumption is only valid for specific contrast agents exhibiting a constant $\partial R_1 / \partial B_0$ within the imaging region of the dreMR magnetic field shifts ($\pm \Delta B$).

$$R_{1\pm} = R_1 \pm \Delta R_1, \text{ assuming a constant } \frac{\partial R_1}{\partial B_0} \quad (2.10)$$

$$I_{Sub} \approx k M_0 \cdot [(1 - \exp(-\Delta t \cdot (R_1 - \Delta R_1))) - (1 - \exp(-\Delta t \cdot (R_1 + \Delta R_1)))] \quad (2.11)$$

$$I_{Sub} \approx k M_0 \cdot [-(\exp(\Delta t \cdot \Delta R_1) \cdot \exp(-\Delta t \cdot R_1)) + (\exp(-\Delta t \cdot \Delta R_1) \cdot \exp(-\Delta t \cdot R_1))] \quad (2.12)$$

$$I_{Sub} \approx 2k M_0 \cdot \sinh(\Delta t \cdot \Delta R_1) \cdot \exp(-\Delta t \cdot R_1) \quad (2.13)$$

The equation quantifies the dreMR contrast intensity in a particular voxel after subtraction in terms of physical parameters such as R_1 , Δt , and the change in R_1 . The hyperbolic sine term accounts for the characteristic contrast produced by the dreMR method. The exponential decay function accounts for the inherent loss of contrast that occurs when the longitudinal relaxation time is set too long such that the voxel magnetizations of the images begin to saturate.

The second method involves a single T_1 -weighted sequence referred to as Double Inversion Recovery (DIR) dreMR pulse sequence (dreMR-DIR) (see Fig. 2.2). Similar to conventional inversion recovery sequences, where signal intensities from tissue with specific relaxation rates are suppressed based on inversion times, the dreMR-DIR pulse sequence suppresses signals arising from tissues without a relaxation rate magnetic field dependence, $\partial R_1/\partial B_0$ (4). During the preparatory stage of the pulse sequence, two field-shifting pulses and two RF 180° inversion pulses are applied to maximize the image contrast for dependence of $\partial R_1/\partial B_0$ and minimize it for dependence of R_1 at the end of the preparatory stage of the pulse sequence (start of the imaging sequence). The dreMR-DIR sequence therefore directly measures the relaxation rate magnetic field dependence and does not require any image post processing.

2.4 Phantom Preparation

MRI phantoms (Fig. 2.6) were prepared for analysis using the dreMR pulse sequences. The samples contained various concentrations of Ablavar and rabbit serum albumin and were all dissolved in $1\times$ phosphate buffer saline (PBS), pH of 7.4 (KH_2PO_4 1.06 mM, NaCl 155.17 mM, $\text{Na}_2\text{HPO}_4\cdot 7\text{H}_2\text{O}$ 2.97 mM) (Product Code 10010023, Gibco, Invitrogen, Burlington, ON, Canada). The rabbit serum albumin (RSA) was purchased as a lyophilized powder, essentially globulin free (~99 %) (Sigma-Aldrich, lot #117K7565V, agarose gel electrophoresis).

The phantom (Fig. 2.6) was prepared in a grid-like fashion with various sample concentrations of RSA and Ablavar. Samples from left to right contained increasing concentrations of RSA dissolved in PBS: 0 μM , 50 μM , 100 μM , 350 μM , and 700 μM .

Samples from top to bottom contained increasing concentrations of Ablavar dissolved in PBS: 0 μM , 50 μM , 100 μM , 250 μM , 500 μM , and 1000 μM .

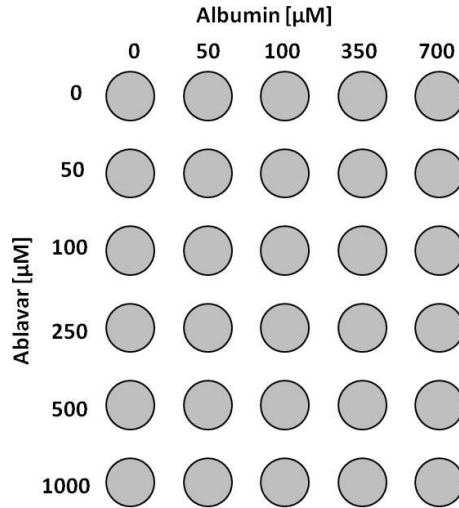


Figure 2.6 The arrangement of samples in the phantom. Samples from left to right contained increasing concentrations of RSA, ranging from 0 to 700 μM . Samples from top to bottom contained increasing concentrations of Ablavar, ranging from 0 to 1000 μM .

2.5 Field-Cycling Relaxometry

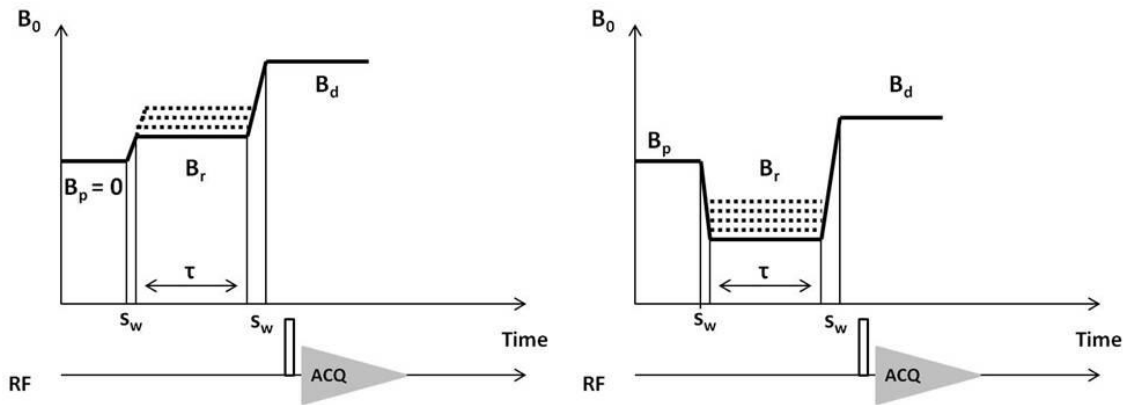


Figure 2.7 Basic Nonpolarized and Prepolarized sequence. The upper trace shows the switching of field values between the fixed polarization field (B_p), the variable relaxation field (B_r), and the fixed detection field (B_d), whereas the bottom trace shows the RF pulse followed after a small delay by the FID acquisition.

DreMR contrast is derived from the relaxivity magnetic field dependence of the bound targeted MR contrast agent. The characteristic high relaxivity magnetic field dependence of bound paramagnetic contrast agents enables suppression of tissue contrast from unbound agents and unenhanced tissue, thereby increasing probe specificity. Ablavar binds specifically to serum albumin and has a strong magnetic field dependence for serum albumin around 1.5T (1, 8, 19). A sample of 80- μ M Albavar dissolved in 4% w/v RSA was measured and acquired using nuclear magnetic resonance dispersion (NMRD) data for magnetic field strengths ranging from 0.010 MHz (0.23 mT) to 42.49 MHz (1.0 T), using a SpinMaster FFC2000 1T C/DC (Stelar s.r.l., Italy) fast field-cycling nuclear magnetic resonance relaxometer. Typical methods to measure T_1 -dispersion profiles (plots of longitudinal relaxation times as a function of field intensity at a constant temperature) at variable field strengths below 1 T are the prepolarized sequence (PP), appropriate for low relaxation fields (B_r), and the nonpolarized sequence (NP), appropriate at higher relaxation fields (Fig. 2.5). The pulse sequence comprised of the NP and PP sequences with a crossover field of 12 MHz (i.e. the relaxation field at which the sequence switches from NP to PP). The sequences were automated experiments designed to measure the longitudinal relaxation rate (R_1) at a given relaxation field. For every given B_r , the FID signal was measured as a function of the time interval tau (τ) (variable relaxation interval), keeping the other (switching, recycle delay, polarization, acquisition) times constant. The NP and PP were comprised of the same systematic setup, the only difference was that the NP sequence had a polarization field set to zero ($B_p = 0$). Each sequence block FID acquisition started with a recycle delay set to ten times the maximum T_1 ($10 \cdot T_{1max}$), followed by a balancing time of $4 \cdot T_{1max} - \tau$, to balance

thermal dissipation in the magnet. The relaxometer cycled to the polarization field of 30 MHz for a time of $4 \cdot T_{1max}$ to reach a steady state of magnetization, then cycled to the relaxation field (B_r) for an interval time of τ . The relaxometer finally cycled to the acquisition field of 16.2 MHz, after which a 90° RF pulse was applied and the FID signal was acquired. The sequence was repeated for 16 blocks, with a decreasing relaxation interval (τ), to calculate the relaxation time at the specific relaxation field with an automated multiblock non-linear, least squares fit. The process was repeated for 30 points (determined by the relaxometer on a logarithmic scale) to complete the T_1 -dispersion profile.

At higher field strengths, an insertable field-cycling relaxometer system (MRIn, Stelar s.r.l., Italy) was used to acquire NMRD curves for ± 0.25 T field shifts about the clinical field strengths of 1.5 T. An Inversion Recovery sequence was used, similar to the PP sequence, except the relaxometer cycled to the acquisition field after the polarization field and applied a 180° RF pulse before cycling to the relaxation field. The polarization and acquisition fields of the insertable field-cycling relaxometer were set to zero corresponding to a Larmor frequency of 63.86 MHz at 1.5T.



Figure 2.8 NMRD data was acquired using the Spinmaster FFC2000 1T C/DC (Stelar s.r.l., Italy) and MRIn equipment. NMRD data for magnetic field strengths ranging from 0.010 MHz to 42.49 MHz was acquired using the SpinMaster relaxometer (Top Left). Top Right and Bottom Row: The insertable field-cycling relaxometer system (MRIn, Stelar s.r.l., Italy) used to acquire NMRD curves for ± 0.25 T field shifts about the clinical field strengths of 1.5 T (Top Right and Bottom Row).

The relaxation rates for the contrast agent solution of 80 μM Albavar dissolved in 4% w/v RSA was measured and acquired ($R_{1,agent}$) and the plain buffer solvent ($R_{1,buffer}$) were recorded for computing the relaxivity (r_1) of the contrast agent,

$$R_{1,agent} = r_1[CA] + R_{1,buffer} \quad (2.14)$$

where $[CA]$ represents the concentration of the contrast agent sample on a per gadolinium ion basis. The estimated R_1 error interval was 2% or less. Samples were maintained at 37°C for all measurements using heated air.

Longitudinal relaxation was modeled using a modification of the Solomon-Bloembergen-Morgan theory formulated by R. Lauffer (9). Contributions to spin-lattice relaxation from the inner hydration sphere were calculated as:

$$\left[\frac{1}{T_1} \right]_{IS} = \frac{[M]}{[H_2O]} \frac{q_{IS}}{T_{1M} + \tau_m} \quad (2.15)$$

where $[1/T_1]_{IS}$ was the spin-lattice relaxation rate due to inner-sphere interactions, $[M]$ was the molar concentration of the paramagnetic species, $[H_2O]$ was the molar concentration of water, q_{IS} was the inner-sphere hydration number, T_{1M} was the relaxation time for bound inner-sphere water molecules, and τ_m was the water residency time.

The inner sphere spin-lattice relaxation rate, including dipolar and contact interactions, was estimated using:

$$\begin{aligned} \frac{1}{T_{1M}} = & \left(\frac{2}{15} \right) \left(\frac{\mu_0}{4\pi} \right)^2 \frac{\gamma_H^2 g_e^2 S(S+1) \mu_B^2}{r_{GdH}^6} \left[\frac{3\tau_c}{1 + \omega_H^2 \tau_c^2} + \frac{7\tau_c}{1 + \omega_S^2 \tau_c^2} \right] \\ & + \frac{2}{3} S(S+1) \left(\frac{A}{\hbar} \right)^2 \left[\frac{\tau_e}{1 + \omega_S^2 \tau_c^2} \right] \end{aligned} \quad (2.15)$$

where μ_0 was the magnetic permeability of vacuum, γ_H was the gyromagnetic ratio for protons, g_e was the electronic g-factor, S was the total electronic spin for the metal ion, μ_B was the Bohr Magneton, r_{GdH} was the metal ion-proton separation and $\frac{A}{\hbar}$ was the electron-nuclear hyperfine coupling constant. ω_H and ω_S were the proton and electron Larmor precessional frequencies (rad/s) in the applied magnetic field respectively.

The dipole-dipole correlation time, τ_c , was calculated from the longitudinal electronic spin relaxation time, T_{1e} , the water residency time, τ_m and the rotational correlation time, τ_R , as follows:

$$\frac{1}{\tau_c} = \frac{1}{T_{1e}} + \frac{1}{\tau_m} + \frac{1}{\tau_R}. \quad (2.16)$$

The longitudinal electronic spin relaxation rate is parameterized as:

$$\frac{1}{T_{1e}} = B \left[\frac{1}{1 + \omega_S^2 \tau_v^2} \right] \text{ where } B = \frac{1}{5\tau_{S0}}. \quad (2.17)$$

Finally, the scalar relaxation time, τ_e , was determined by:

$$\frac{1}{\tau_e} = \frac{1}{T_{1e}} + \frac{1}{\tau_m}. \quad (2.18)$$

2.6 Animal Preparation

The animal experiments were approved by the Animal Use Subcommittee of the University Council on Animal Care at The University of Western Ontario following the guidelines of the Canadian Council on Animal Care (protocol number 2010-210 and 2011-085) (Appendix B and C).

A total of three mice were used, all following the same preparation, anesthesia, and injection protocols for imaging. Two cancer model mice were used for the dreMR subtraction method, and one healthy mouse was used for the dreMR-DIR method.

The mice were initially anesthetized with 5% Isoflurane (Baxter Corporation, Mississauga, ON, Canada) with a vaporizer (VetEquip, Pleasanton, CA, USA) in an induction chamber. The mice were fitted with a breathing rate monitor (Small Animal Instruments Inc., Stony Brook, NY, USA) to monitor the breathing rates under anesthesia and then transferred to a custom water-heated mouse bed where Isoflurane was administered (reduced to 2% with O₂) through a nose cone. The Isoflurane concentration was adjusted between 1-3% during the imaging session based on breathing rate. The water temperature of the mouse bed was controlled to body temperature with a T/Pump (Gaymar, Torrington, CT, USA). The mice were injected by tail-vein with a bolus of Ablavar diluted in saline at a dose of 100 μ M/kg. The two cancer model mice were

sacrificed using Euthanyl Forte (Pentobarbital Sodium Injection) at a dose of 2 mL/kg (Bimeda-MTC Animal Health Inc, Cambridge, ON, Canada).

2.6.1 Prostate Cancer model

PC-3M cells (NCI, Frederick, MD, USA) were cultured in RPMI-1640 supplemented with 10% fetal bovine serum (FBS) (Gibco, Invitrogen, Burlington, ON, Canada). All cells were maintained at 37 °C and 5% CO₂. Two million PC-3M cells suspended in 100 µL Hank's Balanced Salt Solution (HBSS) (Gibco, Invitrogen, Burlington, ON, Canada) were injected subcutaneously in the right and left flanks of a female (19 g) nude mouse (nu/nu; Charles River Laboratories, QC, Canada) at day 0 (50). The mouse was imaged on day 28.

2.6.2 Breast Cancer model

MDA-MB-231 cells (ATCC, Manassas, VA, USA) were cultured in Dulbecco's modified Eagle's medium (DMEM) supplemented with 10% FBS. All cells were maintained at 37 °C and 5% CO₂. One million MDA-MB-231 cells suspended in 50-µL HBSS were injected into the mammary fat pad on the left side of a female (18 g) nude mouse (nu/nu; Charles River Laboratories, QC, Canada) at day 0. The mouse was imaged on day 29.

2.7 Magnetic Resonance Acquisition and Image Processing

The dreMR pulse sequence was a custom-built sequence based on a standard imaging sequence known as the Triple Inversion Recovery. The pulse sequence consisted

of a preparatory stage, whereby the ΔB magnetic field shifts were applied, followed by imaging acquisition. The ΔB magnetic field shifts were applied for each row of k -space and were timed to end 2 ms prior to image acquisition. The dreMR subtraction method takes the normalized difference of the field-shifted images: positive field shifted images (I_+), and negative field shifted images (I_-). The raw data for all images were acquired to perform the image processing. The data sets were first normalized (to remove the influences of the changing equilibrium magnetization) and scaled (if there were multiple images were taken). A subtraction-based pixel by pixel phase correction was then applied to minimize the effects phase shifts induced by the eddy currents. The phase difference of the k -space data from the I_+ and I_- data sets was calculated and applied to one of the data sets (either I_+ or I_-). A complex subtraction of the I_+ and I_- data sets calculated before obtaining the final magnitude dreMR image. The double inversion recovery dreMR sequence required no image processing. All the image processing was performed using Matlab 2012 tools (MathWorks, Natick, Massachusetts, U.S.A.)

2.8 Magnetic Resonance Imaging

2.8.1 Phantoms

The fast spin-echo pulse sequence parameters used to produce the dreMR images using the dreMR subtraction method were: 1000-ms pulse repetition time, 12.08-ms echo time, echo train length of two, 122 Hz per pixel, one average, isotropic in-plane resolution of 0.27 mm, and 15-mm slice thickness. The matrix size was 256×256. The main magnetic field was modulated ± 0.221 T with preparatory dreMR pulse of 500-ms duration. The ΔB pulses were timed to end 2 ms prior to image acquisition.

The dreMR-DIR (Double Inversion Recovery) sequence parameters used to produce the dreMR images using the dreMR DIR method were: : 450-ms pulse repetition time, 6.904-ms echo time, 50-ms inversion time, echo train length of two, 122 Hz per pixel, one average, isotropic in-plane resolution of 0.55 mm, and 8-mm slice thickness. The matrix size was 128×128. The main magnetic field was modulated with preparatory dreMR pulse durations of a 50-ms P1 time, a P2 time of 150 ms with a positive 0.221-T magnetic field shift, and a P3 time of 50 ms with a negative 0.221-T magnetic field shift. The ΔB pulses were timed to end 2 ms prior to image acquisition.

2.8.2 *In vivo* Research

2.8.2.1 Prostate Cancer Model

The fast spin-echo pulse sequence parameters used to produce the axial dreMR images using the dreMR subtraction method were: 500-ms pulse repetition time, 9.376-ms echo time, echo train length of two, 81 Hz per pixel, one average, isotropic in-plane resolution of 0.39 mm, and 4-mm slice thickness. The matrix size was 128×128. The main magnetic field was modulated ± 0.221 T with preparatory dreMR pulses of 300-ms duration. The ΔB pulses were timed to end 2 ms prior to image acquisition. Nine data sets were averaged to produce the resulting dreMR image. Two 4-mm-diameter NMR vials containing 160 μM of Ablavar loaded with and without 4.0% w/v RSA were placed within the imaging region of the tumours to serve as dreMR contrast controls. T_1 - and T_2 -weighted were also obtained before and after Ablavar was injected into the animal.

2.8.2.2 Breast Cancer Model

The fast spin-echo pulse sequence parameters used to produce the axial dreMR images using the dreMR subtraction method were: 500-ms pulse repetition time, 9.376-ms echo time, echo train length of two, 81 Hz per pixel, one average, isotropic in-plane resolution of 0.39 mm, and 4-mm slice thickness. The matrix size was 128×128. Ten data sets were averaged to produce the resulting dreMR image. The fast spin-echo pulse sequence parameters used to produce the coronal dreMR images using the dreMR subtraction method were: 500-ms pulse repetition time, 8.512-ms echo time, echo train length of two, 81 Hz per pixel, 10 averages, in-plane resolution of 0.93x0.38 mm, and 4-mm slice thickness. The main magnetic field was modulated ± 0.221 T with preparatory dreMR pulses of 300 ms in duration. The ΔB pulses were timed to end 2 ms prior to image acquisition. Two 4-mm-diameter NMR vials containing 160 μ M of Ablavar loaded with (labeled 2) and without (labeled 1) 4.0% w/v RSA were placed within the imaging region of the tumours to serve as dreMR contrast controls. T_1 - and T_2 -weighted were also obtained before and after Ablavar was injected into the animal.

2.8.2.3 Healthy Mouse – DIR sequence

The dreMR-DIR (Double Inversion Recovery) sequence parameters used to produce the dreMR images using the dreMR DIR method were: 450-ms pulse repetition time, 6.744-ms echo time, 50-ms inversion time, echo train length of two, 122 Hz per pixel, five averages, isotropic in-plane resolution of 0.70 mm, and 2-mm slice thickness. The matrix size was 128×128. The main magnetic field was modulated with preparatory dreMR pulse durations of a 100-ms P1 time, a P2 time of 100 ms with a positive 0.221-T

magnetic field shift, and a P3 time of 90 ms with a negative 0.221-T magnetic field shift. The ΔB pulses were timed to end 2 ms prior to image acquisition. Two 4-mm-diameter NMR vials containing 160 μM of Ablavar loaded with (2) and without (1) 4.0% w/v RSA were placed within the imaging region of the tumours to serve as dreMR contrast controls. T_1 -weighted images were obtained, prior to Ablavar injection, to overlay the dreMR-DIR image.

Chapter 3

Results

In Chapter 3, the relaxation rates of 80- μ M Albavar dissolved in 4% w/v RSA were measured for magnetic field strengths ranging from 0.010 MHz (0.23 mT) to 42.49 MHz (1.0 T), and an insertable field-cycling relaxometer system was used to acquire NMRD curves for ± 0.25 T field shifts about the clinical field strengths of 1.5 T. The relaxometry data analysis demonstrated the basis by which the dreMR contrast is derived during MR imaging. dreMR imaging was performed using the single inversion subtraction method and the double inversion recovery method. Phantoms and *in vivo* mouse models were used for both dreMR imaging methods, and the resulting dreMR contrast images are shown. The appropriate image post-processing are implanted to correct for the necessary field normalization and phase corrections for the single inversion subtraction based method.

3.1 Relaxometry Data - Fitting Results Using Lauffer Model of

Relaxivity

T_1 dispersion experiments were conducted to measure the field dependence of NMR spin-lattice relaxation times of 80- μ M Ablavar with and without RSA from 10 kHz to 64 MHz (NMRD profiles) using the SpinMaster FFC2000 1T C/DC and MRIn relaxometers. The red line (Fig. 3.1 A and B) indicates the imaging region of interest. dreMR is able to exploit the characteristic high relaxivity magnetic field dependence of

the bound paramagnetic contrast agent about 1.5 T (63.86 MHz) to produce image contrast that is proportional to the concentration of the targeted contrast agent. The significant change in relaxivity between the bound (Fig. 3.1 A) and unbound (Fig. 3.1 B) contrast agent is noted in the change in scale of the two graphs below.

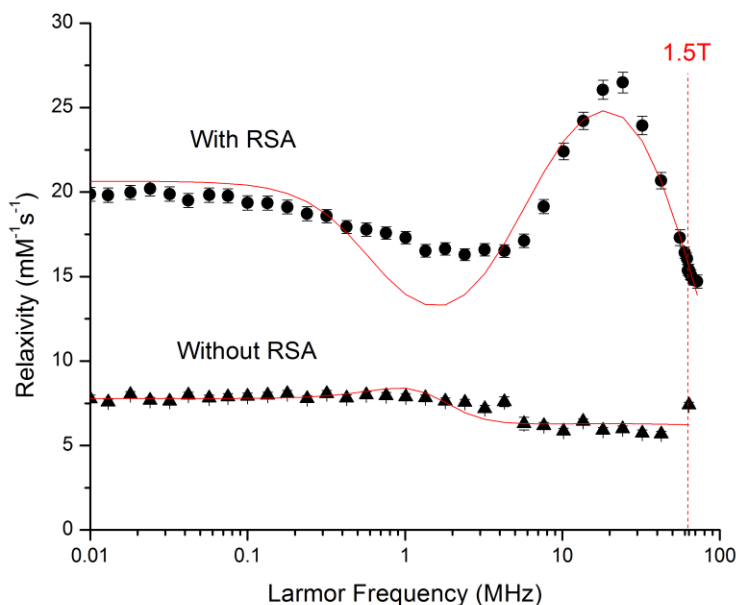


Figure 3.1 Fitting Results Using Lauffer Model of Relaxivity for 80- μM sample of Ablavar measured at 37°C. The Lauffer model for inner-sphere dipole-dipole relaxation (red trace) has been fit to relaxivities derived from NMRD data at 37°C. (circles) Sample with 4% w/v Rabbit Serum Albumin. (triangles) No Rabbit Serum Albumin.

Table of Fitting Results

Table 1. Longitudinal relaxation model using a modification of the Solomon-Bloembergen-Morgan theory formulated by R. Lauffer. The fitted parameters and their uncertainties (one standard deviation) are given in the following table.

Parameter	Units	Ablavar with RSA	Ablavar
		37°C	37°C
τ_v	ps	38.4 ± 4.2	102.0 ± 14
τ_R	ns	5.72 ± 0.59	0.24 ± 0.01
τ_m	ns	552 ± 19	552 (fixed)
τ_{S0}	ps	578 ± 50	154.3 ± 5.9
A/\hbar	rad/s	$3 \cdot 10^6$ (fixed)	$3 \cdot 10^6$ (fixed)
r_{GdH}	pm	0.31 (fixed)	0.31 (fixed)
q_{IS}	-	1 (fixed)	1 (fixed)

τ_v : Correlation time for modulation of the transient zero-field splitting, τ_R : Rotational correlation time, τ_m : Water residency time, τ_{S0} : Electronic relaxation time at zero field, A/\hbar : electron-nuclear hyperfine coupling constant, r_{GdH} : metal ion-proton separation, q_{IS} : inner-sphere hydration number

3.2 Phantom Images

3.2.1 dreMR Single Inversion subtraction

A phantom study was conducted in which the dreMR single inversion subtraction method was implemented to produce a dreMR image. The method required the weighted subtraction of two T_1 -weighted images with ± 0.221 T dreMR magnetic field shifts, one with a positive (T_{1+}) and the other with a negative (T_{1-}) magnetic field shift during the preparatory stage of the pulse sequence. Subtraction of the T_{1+} and T_{1-} images produce an image where the contrast intensity was due to the magnetic field dependence of the targeted contrast agent. Phantoms (Fig. 3.2) were prepared in a grid-like fashion with various sample concentrations of RSA and Ablavar in order to test the proposed method without any physiological effects. The resulting dreMR image is presented as a false-colour image.

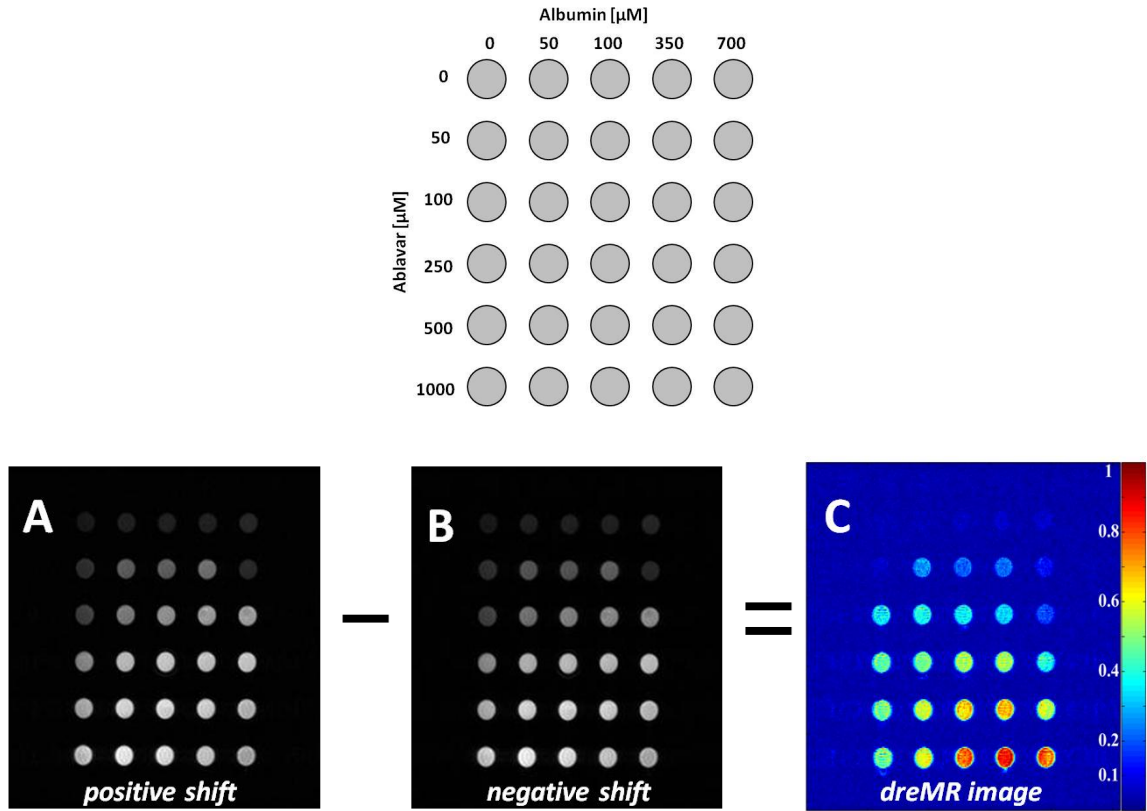


Figure 3.2 Phantom and MRI images. Top: Arrangement of the samples in the phantom. Samples from left to right contained increasing concentrations of RSA, ranging from 0 to 700 μM . Samples from top to bottom contained increasing concentrations of Ablavar, ranging from 0 to 1000 μM . Bottom: Subtraction of the T_1 -weighted images. Images A and B show the T_1 -weighted images using the dreMR pulse sequence with positive (A) and negative (B) field shifts of 0.221 T. Image C shows the resulting dreMR image using the dreMR subtraction method.

3.2.2 dreMR Double Inversion Recovery

A phantom study was conducted in which the dreMR Double Inversion Recovery method was implemented to produce a dreMR image. Similar to conventional inversion recovery sequences, where signal intensities from tissue with specific relaxation rates are suppressed based on inversion times, the dreMR-DIR pulse sequence suppresses signals arising from tissues without a relaxation rate magnetic field dependence and therefore required no image processing. Phantoms (Fig. 3.3 A) were prepared in a grid-like fashion with various sample concentrations of RSA and Ablavar in order to test the proposed method without any physiological effects. A T_1 -weighted image (Fig. 3.3 B) was acquired using a standard fast spin-echo pulse sequence to observe and measure the resulting contrast from the dreMR-DIR image (Fig. 3.3 C). The dreMR-DIR image is presented as a grayscale image to compare with the standard FGRE sequence. The samples with the lowest concentrations of Ablavar and RSA exhibit limited signal intensities, while the samples with the larger concentrations of Ablavar and RSA show increased signal intensities.

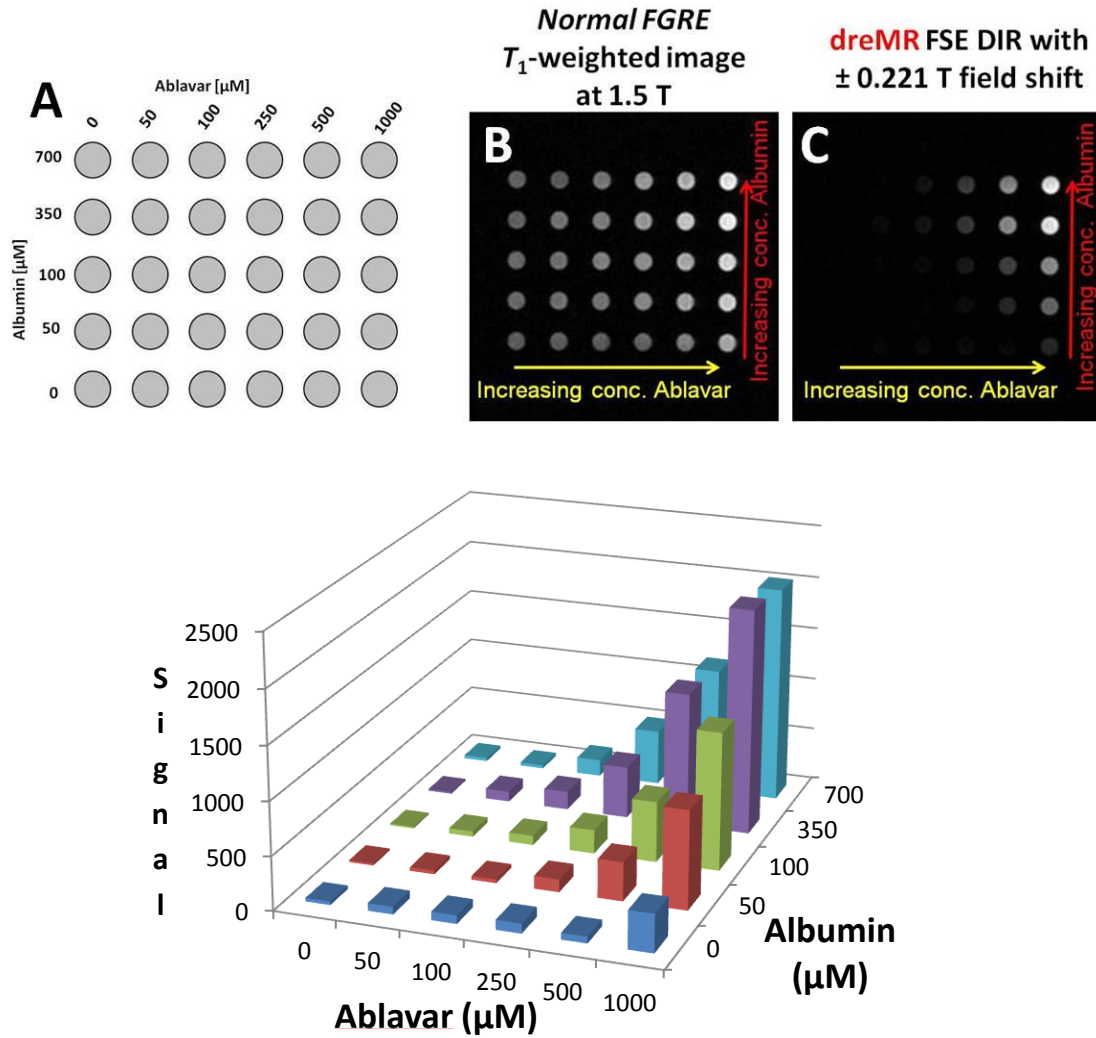


Figure 3.3 Phantom and MRI images. Top: (A) Arrangement of the samples in the phantom. Samples from bottom to top contained increasing concentrations of RSA, ranging from 0 to 700 μM . Samples from left to right contained increasing concentrations of Ablavar, ranging from 0 to 1000 μM . (B) T_1 -weighted image using a standard fast gradient echo pulse sequence acquired at 1.5 T (no field shifting). (C) Image shows the resulting dreMR image acquired with the dreMR-DIR sequence. The dreMR-DIR method demonstrates the ability to both suppress and enhance signal intensities of various albumin concentrations bound to various Ablavar concentrations without any post processing.

3.3 *In vivo* Images

3.3.1 Prostate Cancer Model

An *in vivo* study was conducted in which the dreMR single inversion subtraction method was implemented to produce a dreMR image. The method required the weighted subtraction of two T_1 -weighted images with ± 0.221 T dreMR magnetic field shifts, one with a positive (T_{1+}) and the other with a negative (T_{1-}) magnetic field shift during the preparatory stage of the pulse sequence. Subtraction of the T_{1+} and T_{1-} images produce an image where the contrast intensity was due to the magnetic field dependence of the targeted contrast agent. A female NU/NU mouse was injected with the human prostate cancer cell line PC-3M and developed tumours on both flanks. The mouse was imaged 28 days post PC-3M cell injections. Two 4-mm NMR vials containing 160 μ M of Ablavar loaded with and without 4.0%w/v RSA were placed within the imaging region of the tumours to serve as dreMR contrast controls. Axial T_1 -weighted images pre- (Fig. 3.4 A) and post-injection (Fig. 3.4 B) of albumin-targeted gadolinium contrast agent (Ablavar), and axial T_2 -weighted image (Fig. 3.4 C) post-injection were taken and indicated a significant tumour volume. Axial T_1 -weighted subtracted images of post- and pre-injection of Ablavar (false colour (3.4 D) and grayscale (3.4 E)) were taken to indicate regions where gadolinium was present. Subtraction of the T_{1+} and T_{1-} images produced a dreMR image (Fig. 3.4 F). Taking advantage of the intrinsic T_1 dispersion of the unenhanced tissues and non-targeted contrast agents, the dreMR single inversion subtraction method produced contrast arising only from signal enhancement of tissues by only the bound form of targeted contrast agent. The resulting dreMR image is presented as a false-colour image.

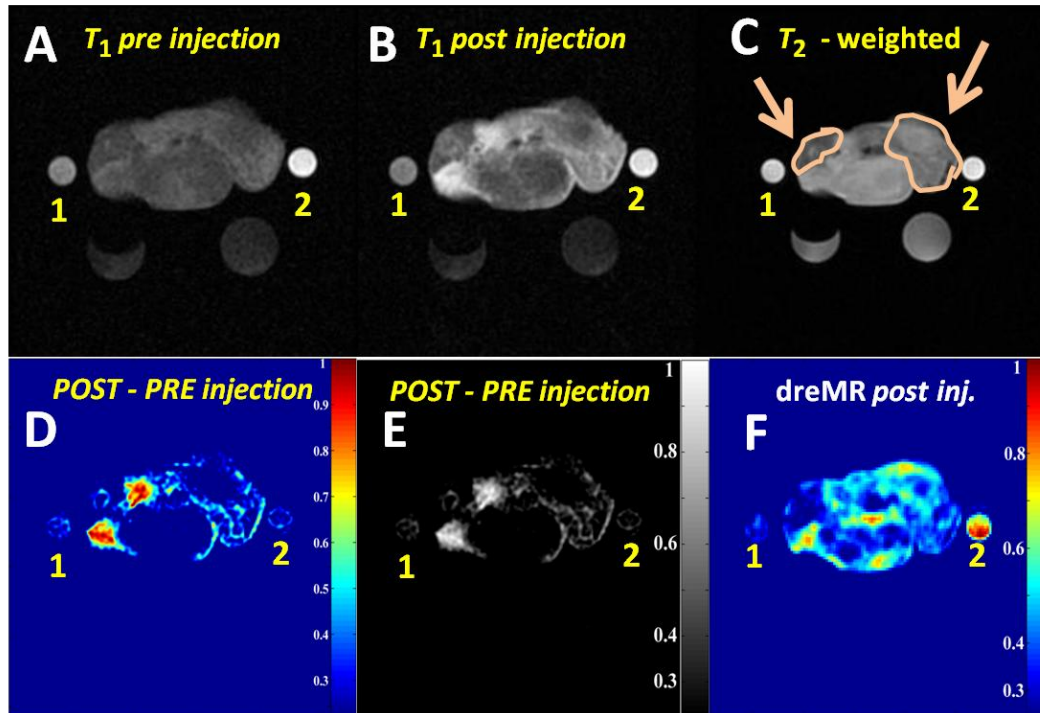


Figure 3.4 Axial image of a female NU/NU mouse under study that developed prostate cancer tumours on both flanks and imaged 28 days post PC-3M cell injections. Two 4-mm NMR vials containing 160 μM of Ablavar loaded (2) with and (1) without 4.0% w/v RSA were placed within the imaging region of the tumours to serve as dreMR contrast controls. Top: (A and B) T_1 -weighted images pre- and post-injection of Ablavar. (C) T_2 -weighted image indicating significant tumour volume. The tumours are demarcated and indicated with the arrows. Bottom (D and E). T_1 -weighted subtracted images of post- and pre-injection of Ablavar ((D) and (E)) indicate regions where gadolinium was present. (F) Resulting dreMR axial image using the dreMR subtraction method. Notice the dramatic change in contrast from the standard pre- and post-injection subtracted images compared to the dreMR image. The contrast from the dreMR image shows only signal intensities arising from the bound form of Ablavar and albumin.

3.3.2 Breast Cancer Model

An *in vivo* study was conducted in which the dreMR single inversion subtraction method was implemented to produce a dreMR image. The method required the weighted subtraction of two T_1 -weighted images with ± 0.221 T dreMR magnetic field shifts, one with a positive (T_{1+}) and the other with a negative (T_{1-}) magnetic field shift during the preparatory stage of the pulse sequence. Subtraction of the T_{1+} and T_{1-} images produce an image where the contrast intensity was due to the magnetic field dependence of the targeted contrast agent. A female NU/NU mouse was injected with the human breast cancer cell line MDA-MB-231 and developed a tumour in the mammary fat pad on the left side. The mouse was imaged 29 days post MDA-MB-231 cell injections. Two 4-mm NMR vials containing 160 μM of Ablavar loaded with and without 4.0% w/v RSA were placed within the imaging region of the tumours to serve as dreMR contrast controls. Axial T_1 -weighted images pre- (Fig. 3.5 A) and post-injection (Fig. 3.5 B) and coronal (Fig. 3.5 F) of albumin-targeted gadolinium contrast agent (Ablavar), and axial T_2 -weighted image (Fig. 3.5 C) post-injection were taken and indicated significant a tumour volume. Subtraction of the T_{1+} and T_{1-} images pre- (Fig. 3.5 D) and post-injection (Fig. 3.5 E and 3.5 F) of Ablavar produced an axial and coronal dreMR images. Taking advantage of the intrinsic T_1 dispersion of the unenhanced tissues and non-targeted contrast agents, the dreMR single inversion subtraction method produced contrast arising only from signal enhancement of tissues by only the bound form of targeted contrast agent. The resulting dreMR images are presented as a false-colour image.

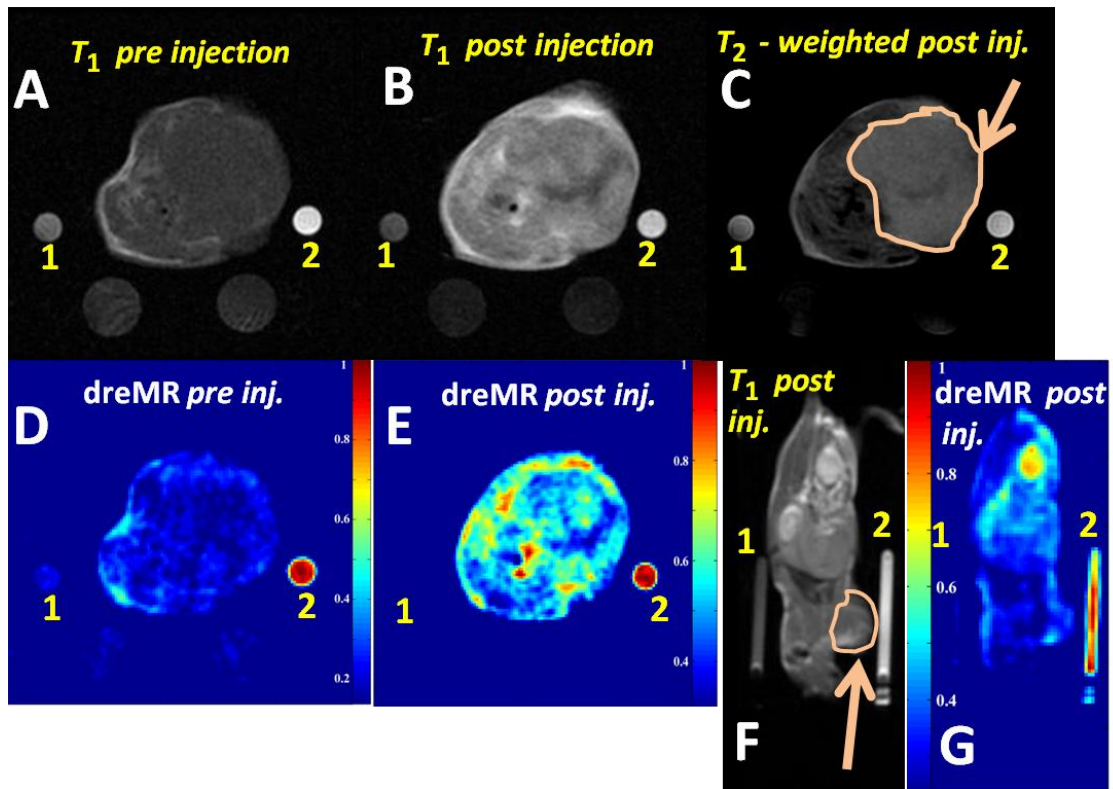


Figure 3.5 Axial and coronal images of a female NU/NU mouse under study that developed a large breast cancer tumour in the mammary fat pad and imaged 29 days post MDA-MB-231 cell injections. Two 4-mm NMR vials containing 160 μ M of Ablavar loaded (2) with and (1) without 4.0% w/v RSA were placed within the imaging region of the tumours to serve as dreMR contrast controls. Top: (A and B) T_1 -weighted images pre- and post-injection of albumin-targeted gadolinium contrast agent (Ablavar). (C) T_2 -weighted image indicating significant tumour volume. The tumours are demarcated and indicated with the arrows. Bottom (D and E). Resulting dreMR axial image using the dreMR subtraction method of (D) pre- and (E) post-injection of Ablavar. (F) T_1 -weighted post-injection coronal images with the tumour demarcated. (G) Resulting dreMR coronal image using the dreMR subtraction method post-injection of Ablavar. The significant change in contrast from the dreMR image shows only signal intensities arising from the bound form of Ablavar and albumin.

3.3.3 Double Inversion Recovery

An *in vivo* study was conducted in which the dreMR Double Inversion Recovery method was implemented to produce a dreMR image. Similar to conventional inversion recovery sequences, where signal intensities from tissue with specific relaxation rates are suppressed based on inversion times, the dreMR-DIR pulse sequence suppresses signals arising from tissues without a relaxation rate magnetic field dependence and therefore required no image processing. Two 4-mm NMR vials containing 160 μM of Ablavar loaded with and without 4.0% w/v RSA were placed within the imaging region of the tumours to serve as dreMR contrast controls. A standard T_1 -weighted image (Fig. 3.6 A) image using a standard fast gradient echo pulse sequence acquired at 1.5 T (no field shifting) was taken to overlay the dreMR-DIR image (Fig. 3.6 B). The dreMR-DIR image was acquired with the magnetic field shifting parameters of 100-ms positive 0.221-T magnetic field shift (P2 Time) and 90-ms negative 0.221 T magnetic field shift observe and measure the resulting dreMR-DIR image (Fig. 3.6 B). The dreMR-DIR image is presented as a false-colour image overlaid with the standard FGRE T_1 -weighted image (Fig. 3.6 C).

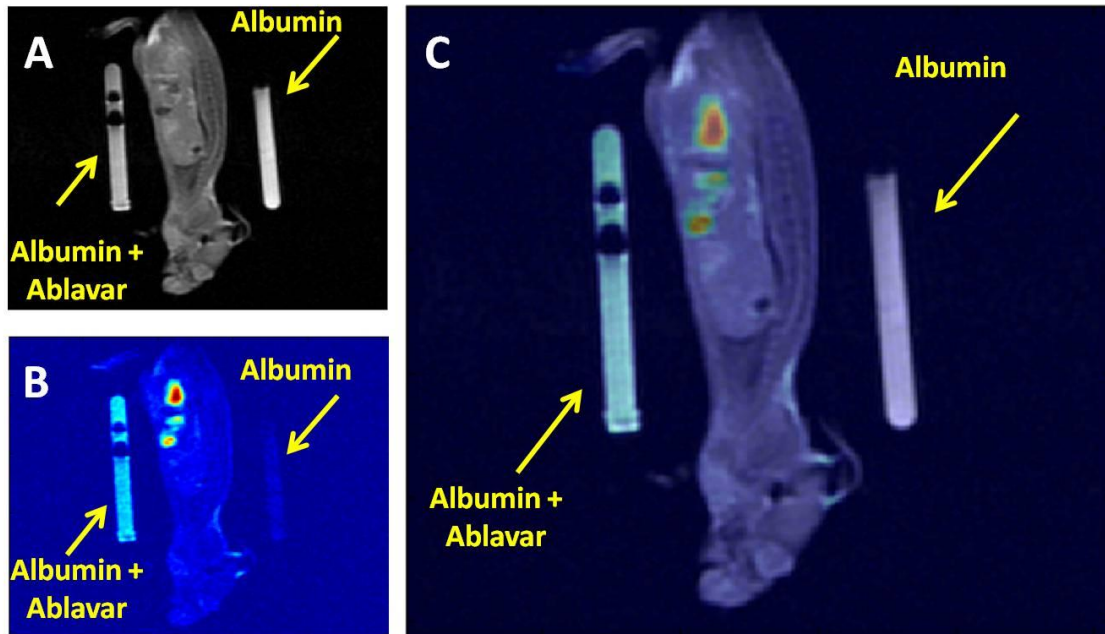


Figure 3.6 Direct albumin imaging using the dreMR Double Inversion Recovery (DIR) pulse sequence. Two 4-mm NMR vials containing 160 μM of Ablavar loaded with and without 4.0% w/v RSA were placed within the imaging region to serve as dreMR contrast controls. Top left (A): T_1 -weighted image using a standard fast gradient echo pulse sequence acquired at 1.5 T. Bottom left (B): dreMR-DIR image with 100-ms positive 0.221 T magnetic field shift (P2 Time) and 90-ms negative 0.221 T magnetic field shift. Right (C): Overlay of dreMR-DIR and T_1 -weighted image. The dreMR-DIR method enables suppression of unbound agents and unenhanced tissues contrast, thereby increasing agent specificity.

Chapter 4

Discussion

4.1 Discussion

Delta Relaxation Enhanced magnetic resonance (dreMR) is an imaging method capable of producing contrast proportional only to the concentration of the bound form of the targetable contrast agent using a dynamic field-cycling technique. The characteristic high relaxivity magnetic field dependence of bound paramagnetic contrast agents enables suppression of unbound agents and unenhanced tissues contrast. The ability to adapt field-cycling relaxometry to MRI increases its sensitivity to image contrast agents with molecular targeting characteristics. The effect of removing the magnetic field shifting pulses during the preparatory phase of the pulse sequence diminishes the ability to distinguish dreMR contrast arising due to the targeted form of the targetable contrast agent. Without the magnetic field shifts, the relaxivity magnetization field dependence cannot be exploited and the contrast would produce a conventional T_1 -weighted image. The dreMR single inversion subtraction and double inversion recovery methods both exploit the relaxivity magnetic field dependence, albeit in different ways.

Using field-cycling relaxometry, it can be seen the relaxation field dependence, $\frac{\partial R_1}{\partial B_0}$, presents strong evidence of contrast agent binding (Fig. 3.1 A and B), evident by the relaxivity dispersion. At 1.5 T, the relaxivity of the targeted and non-targeted contrast

agent with rabbit serum albumin was $16 \text{ mM}^{-1}\text{s}^{-1}$ and $7.5 \text{ mM}^{-1}\text{s}^{-1}$, which was in agreement with values reported in literature (1, 12, 19).

The significance is not the relaxivity at a fixed magnetic field strength, but rather its change with respect to the magnetic field. From the relaxometry data, imaging with the administration of Ablavar at 1.5 T would result in an absolute relaxivity enhancement of 2.1 (ratio of targeted Ablavar to non-targeted Ablavar), whereas the relaxivity slope enhancement ratio was 95 (from 1.25 T to 1.75 T). The large increase of the relaxivity slope enhancement ratio over the absolute relaxivity enhancement of only the targeted form of Ablavar (non-enhanced tissues and non-targeted Ablavar do not demonstrate strong relaxivity field dependences (9, 29)) is what makes dreMR imaging feasible. The phantom experiments demonstrate magnetization can be prepared and produce signal intensities proportional to $\frac{\partial R_1}{\partial B_0}$ using both dreMR imaging techniques (single inversion and double inversion).

The single inversion subtraction dreMR technique required an acquisition of two images acquired with magnetic field shifts, equal in duration and magnitude. The raw data from the field-shifted images are then normalized to remove the influences of the changing equilibrium magnetization through post-processing. Minor inductive coupling between the dreMR B_0 insert coil and the clinical MRI system produce eddy currents in the conductive materials in the MRI system, even with the use of active shielding. The eddy currents create a frequency offset such that there became a shift within the field-of-view along the frequency encoding and slice selection directions. The phase-based correction was meant to correct only the shift in the frequency encoding direction. Eddy currents induced by the rapid switching dreMR B_0 insert coil reduces the quality of the

final dreMR image, therefore a phase-based correction was applied to the positive and negative T_1 -weighted images. The phase difference from the k -space data from the positive and negative field variations were minimized to correct for this observation. After the appropriate field normalizations and phase correction, a complex subtraction of the complex k -space data was performed before obtaining the final magnitude dreMR image. The final dreMR images (refer to Figures. 3.4 F and 3.5 E and G) produced by the subtraction based single inversion dreMR technique produces contrast proportional to $\frac{\partial R_1}{\partial B_0}$, where the magnetic field shifts were created by the dreMR B_0 field-cycling insert coil. The penalty for the single inversion subtraction dreMR technique is a drop-off in SNR, a reduction of approximately 20%, however the gains in probe specificity more than compensate for this drawback.

Prior to injection of Ablavar, the dreMR image (Fig 3.5 D) produced no tissue contrast. Post-injection of Ablavar (Fig 3.4 B, Fig. 3.5 B), the T_1 -weighted images showed an increase in contrast associated with accumulation of Ablavar, however the ability to distinguish contrast arising from the only the targeted form of Ablavar became difficult since contrast from unenhanced tissues and non-targeted Ablavar were still present. A post- *minus* pre-Ablavar injection (Fig. 3.4 D) nicely defined regions where the contrast agent was present; however it was only the final dreMR image that showed regions where Ablavar was targeted to albumin. The *in vivo* dreMR images showed an increase in contrast around the periphery of the tumours (Fig. 3.4 F, Fig. 3.5 E and G). The presence of the two phantoms placed beside the mouse during imaging served as dreMR contrast controls and showed the contrast from the dreMR images were due to

only the targeted form of Ablavar. Without histological examination, characterizations about the tumour and surrounding vascular environment were not feasible.

The double inversion recovery (DIR) dreMR sequence differs from the single inversion subtraction dreMR technique such that the DIR method can directly prepare magnetization based upon $\frac{\partial R_1}{\partial B_0}$ without any image post-processing. During the preparatory section of the dreMR-DIR pulse sequence, two ΔB (± 0.221 T) field-shifting pulses and two 180° RF pulses are applied prior to the start of the image acquisition sequence. The DIR preparatory pulse sequence was similar to standard inversion recovery pulse sequences that were meant to minimize sample magnetization from fat and water (51). The DIR preparatory pulse sequence was applied to maximize the magnetization dependence of $\frac{\partial R_1}{\partial B_0}$ and minimize the magnetization dependence of R_1 before the start of image acquisition (4). The three periods within the preparatory phase (P1 time, P2 time, and P3 time) were optimized for magnetization evolution producing contrast only from $\frac{\partial R_1}{\partial B_0}$ of the targeted form of the Ablavar, and to suppress any contrast resulting from sample tissues and the non-targeted form of Ablavar (4). The $\frac{\partial R_1}{\partial B_0}$ dependence was a strong indication of Ablavar-albumin binding and the dreMR-DIR image presented contrast the localized targeted binding. The resulting image intensity depended on factors including the concentration of albumin and Ablavar, proton density and magnitude of the dreMR magnetic field shift. The dreMR-DIR image of a healthy mouse presented in figure 3.6 B and C, showed dreMR contrast in the kidneys and bladder due to the time differences between the injection of Ablavar and the image acquisition (40 minutes) and fast clearance of the contrast agent.

4.2 Limitations and Future Work

We identified a number of limitations within the scope of the initial *in vivo* dreMR imaging analysis and results that motivate the future direction of dreMR imaging. Areas of interest include: Ablavar bio-distribution and quantification, histological and immunohistochemical characterization of the tumour vascular environment, and improving the dreMR imaging technique.

4.2.1 Ablavar Binding and Relaxivity

The development of Ablavar towards FDA-approval for use as an MRI intravascular contrast agent has been focused and optimized for use in humans (12, 19, 52), and as such, the albumin binding affinities and relaxivities exhibit a species dependence. Ablavar was designed to bind strongly and reversibly with human serum albumin in plasma, allowing for long vascular retention and plasma half-life (52), and an relaxivity increase 6-10 times that of Gd-DTPA (19, 52). However, because the albumin binding is reversible, the relaxivity will depend on dose and time of injection, and species binding affinities. Not only does the total volume fraction albumin vary among species, but the binding affinity for albumin can impact how translatable an animal model to clinical settings is that depends on these factors. The affinity with purified albumin at fixed concentrations exhibit no species dependences, however Ablavar binding in plasma serum albumin is greatest in humans (91%) compared to dogs, rats and mice (~60%) (i.e. binding for HSA > pig SA ~ rabbit SA > dog SA ~ rat SA ~ mouse SA) (20). These factors also impact the relaxivity among species of Ablavar binding in blood plasma (relaxivity in human > pig > dog ~ rabbit ~ rat ~ mouse) (20). The differences in relaxivities of Ablavar across species have been attributed to the protein binding and

changes in the water exchange rate (29, 52, 53). These factors limited the ability for quantification of albumin with the dreMR contrast vials. The dreMR contrast vials used for the *in vivo* murine experiments contained rabbit serum albumin, and while the dreMR image showed contrast for only the targeted form of Ablavar with rabbit serum albumin, it was not possible to make appropriate quantification of the *in vivo* dreMR contrast due to the Ablavar pharmacokinetic species dependence.

Ablavar has previously been used to study different disease states in murine models, including a glioma model to examine contrast enhancement and dose-effectiveness of Ablavar compared to OptiMARK (gadoversetamide), an extracellular gadolinium-based MRI contrast agent (54), and an inflammatory lesion model to examine inflammatory changes in the kidneys that leads to lupus nephritis (53). While the slow buildup and long vascular retention in tumours of Ablavar will lead to contrast enhancement, the use of a murine model will be less representative to predict the behavior of Ablavar in humans. The ability for dreMR to detect the small and sensitive tumour and vascular changes in a murine model would however be scalable for humans, where the binding kinetics and relaxivities of Ablavar are greatest.

4.2.2 Correlation with Histology and Visualizing Vascular

Permeability

An important area of any research using animal models is the correlation of the experimental images with histology and/or immunohistochemistry. Due to the limited number of animals used thus far for the initial dreMR *in vivo* experiments, we were unable to perform appropriate histological characterization of the tumour and surrounding

tumour vascular environment. Through further investigations of the albumin uptake of the tumour and surrounding vascular environment, and by observing and examining the differences of the tissue and tumour morphologies over time, we can begin to understand the changes in contrast observed with the dreMR images. Angiogenesis plays an important role in the progression, growth, and metastasis of tumours (55). The ability to measure, monitor, and understand their underlying molecular mechanisms can impact clinical therapies and patient outcomes. Macromolecular contrast media can provide a means for imaging and quantifying angiogenesis and tumour permeability (56-60). Due to the tendency of tumours to grow vascular networks quickly to feed their large energy demands, angiogenic vessels become permeable to macromolecular contrast media, where as non-diseased vessels do not (55, 61, 62). Albumin has previously been shown to have an increased specificity to tumour development and response to therapies (24, 25, 61, 63). The ability for albumin to extravasate through permeable vessels into tumours makes it useful as a targetable molecule for tumour detection and characterization (61). Histological examinations of the albumin-Ablavar complex can be achieved using fluorescein microscopy of an avidin-biotin complex stain, which would yield a representation of the tumour and tumour vascular permeability (64, 65). Dafni *et. al.* (2003) have previously used triply labeled albumin with biotin, rhodamine, and GdTPA to show the feasibility to detect by histology, fluorescence, MRI, and inductively coupled plasma mass spectrometry the clearance of interstitial macromolecular plasma proteins after their extravasation from permeable blood vessels (66).

4.2.3 Imaging Technique Improvements

The sensitivity of our study was limited primarily by the binding affinities and relaxivities of Ablavar to albumin, but also the ability to apply the appropriate field normalizations to the positive and negative T_1 -weighed images to acquire the dreMR images. Small image-offset errors can create imperfect normalizations and image registrations, reducing the final quality and accuracy of the dreMR image (4, 27, 67, 68). The inability to suppress non-targeted contrast media and native tissues would lead to image artifacts and result in artificial dreMR contrast. The largest source causing image shifting errors was the occurrence of eddy currents induced by the fast switching of the field-cycling dreMR B_0 insert coil. The ability to compensate and correct for the presence of eddy currents eliminates the necessity to insert a delay time period between the preparatory stage of the pulse sequence and start of image acquisition, thereby increasing the available magnetization (created in the preparatory stage of the pulse sequence) for dreMR contrast.

There are two available methods for eddy current compensation: (1) waveform pre-emphasis, and (2) dynamically adjusting the MRI system frequency. Waveform pre-emphasis requires additional hardware implementation, control and synchronization with the imaging pulse sequence, and high fidelity amplifiers (51). Dynamically adjusting the system frequency requires the ability to modulate the pulse sequence before imaging (integrating another preparatory stage to the pulse sequence) to compensate and minimize the offset between the Larmor frequency and system reference frequency (67). Both methods require prior knowledge of the temporal behavior of the eddy current for implementation. Hoelscher *et al.* (67) have recently integrated an eddy current

compensation for dreMR imaging by dynamic phase modulation called eDREAM (Dynamic Reference Phase Modulation). The approach uses a time varying phase that is added to the RF pulse and acquisition window to dynamically correct for the frequency offset. An eddy current compensation with waveform pre-emphasis is currently under investigation to improve the dreMR imaging technique. The approach uses a current-controlled Helmholtz magnet pair wound around the diameter of the dreMR insert coil, which is dynamically synchronized to create a time-varying frequency offset at the end of the dreMR magnetic field shift (immediately before image acquisition) to compensate for the presence of the eddy current.

4.3 Conclusion

The development and application of dreMR for field-cycling contrast was demonstrated for *in vivo* imaging. The overarching theme of this thesis was to extend the previous work of Alford *et. al.* (4) to develop and integrate dreMR towards an *in vivo* diseased animal model. Field-cycling relaxometry techniques were used to measure and characterize the relaxivity of the targeting contrast agent Ablavar, demonstrating a relaxivity magnetic field dependence for only the targeted form with albumin. New dreMR hardware and pulse sequences were synchronized and implemented to examine the Albavar-albumin binding to distinguish only the targeted form of the contrast agent. The dreMR imaging techniques greatly increases the ability to produce MR contrast localized to the sites where Ablavar was targeted with albumin. Imaging with dreMR can produce dreMR contrast by way of two techniques: (1) dreMR single inversion subtraction technique, and (2) dreMR double inversion recovery. Any targetable contrast

media that exhibits relaxivity magnetic field dependence can be utilized with dreMR imaging. Development and understanding of current and emerging biomarkers can be enhanced by the increased specificity of dreMR imaging, which can lead to effective strategies for cancer staging through a new method of molecular imaging.

References

1. Caravan P. Strategies for increasing the sensitivity of gadolinium based MRI contrast agents. *Chemical Society reviews*. 2006;35(6):512-23.
2. McRobbie DW. MRI from picture to proton. 2nd ed. Cambridge, UK ; New York: Cambridge University Press, 2007.
3. Haacke EM. Magnetic resonance imaging : physical principles and sequence design. New York: Wiley, 1999.
4. Alford JK. Delta Relaxation Enhanced Magnetic Resonance [Integrated Article]. University of Western Ontario: University of Western Ontario, 2009.
5. Bushberg JT. The essential physics of medical imaging. 2nd ed. Philadelphia: Lippincott Williams & Wilkins, 2002.
6. Tóth É, Helm L, Merbach A. Relaxivity of MRI Contrast Agents. *Topics in Current Chemistry*. 2002;221:61-101.
7. Weinmann HJ, Ebert W, Misselwitz B, Schmitt-Willich H. Tissue-specific MR contrast agents. *European journal of radiology*. 2003;46(1):33-44.
8. Caravan P, Ellison JJ, McMurry TJ, Lauffer RB. Gadolinium(III) Chelates as MRI Contrast Agents: Structure, Dynamics, and Applications. *Chemical reviews*. 1999;99(9):2293-352.
9. Lauffer RB. Paramagnetic metal complexes as water proton relaxation agents for NMR imaging: theory and design. *Chemical reviews*. 1987;87(5):901-27.
10. Hermann P, Kotek J, Kubicek V, Lukes I. Gadolinium(III) complexes as MRI contrast agents: ligand design and properties of the complexes. *Dalton T*. 2008(23):3027-47.
11. Makowski MR, Wiethoff AJ, Jansen CH, Botnar RM. Molecular imaging with targeted contrast agents. *Topics in magnetic resonance imaging : TMRI*. 2009;20(4):247-59.
12. Caravan P. Protein-targeted gadolinium-based magnetic resonance imaging (MRI) contrast agents: design and mechanism of action. *Accounts of chemical research*. 2009;42(7):851-62.
13. Winter PM, Caruthers SD, Wickline SA, Lanza GM. Molecular imaging by MRI. *Current cardiology reports*. 2006;8(1):65-9.
14. Aime S, Barge A, Gianolio E, Pagliarin R, Silengo L, Tei L. High Relaxivity Contrast Agents for MRI and Molecular Imaging. 2005;49:99-121.
15. Raymond KN, Pierre VC. Next generation, high relaxivity gadolinium MRI agents. *Bioconjugate chemistry*. 2005;16(1):3-8.
16. Sosnovik DE, Weissleder R. Emerging concepts in molecular MRI. *Current opinion in biotechnology*. 2007;18(1):4-10.
17. Terreno E, Castelli DD, Viale A, Aime S. Challenges for molecular magnetic resonance imaging. *Chemical reviews*. 2010;110(5):3019-42.
18. Morawski AM, Lanza GA, Wickline SA. Targeted contrast agents for magnetic resonance imaging and ultrasound. *Current opinion in biotechnology*. 2005;16(1):89-92.
19. Caravan P, Cloutier NJ, Greenfield MT, et al. The interaction of MS-325 with human serum albumin and its effect on proton relaxation rates. *J Am Chem Soc*. 2002;124(12):3152-62.
20. Eldredge HB, Spiller M, Chasse JM, Greenwood MT, Caravan P. Species dependence on plasma protein binding and relaxivity of the gadolinium-based MRI contrast agent MS-325. *Investigative radiology*. 2006;41(3):229-43.
21. Overoye-Chan K, Koerner S, Looby RJ, et al. EP-2104R: a fibrin-specific gadolinium-Based MRI contrast agent for detection of thrombus. *Journal of the American Chemical Society*. 2008;130(18):6025-39.

22. Sullivan DH. What do the serum proteins tell us about our elderly patients? *The journals of gerontology Series A, Biological sciences and medical sciences*. 2001;56(2):M71-4.
23. Yuan F, Chen Y, Dellian M, Safabakhsh N, Ferrara N, Jain RK. Time-dependent vascular regression and permeability changes in established human tumor xenografts induced by an anti-vascular endothelial growth factor/vascular permeability factor antibody. *Proceedings of the National Academy of Sciences of the United States of America*. 1996;93(25):14765-70.
24. Desai N, Trieu V, Damascelli B, Soon-Shiong P. SPARC Expression Correlates with Tumor Response to Albumin-Bound Paclitaxel in Head and Neck Cancer Patients. *Translational oncology*. 2009;2(2):59-64.
25. Schnitzer JE, Oh P. Antibodies to SPARC inhibit albumin binding to SPARC, gp60, and microvascular endothelium. *The American journal of physiology*. 1992;263(6 Pt 2):H1872-9.
26. Chlenski A, Guerrero LJ, Salwen HR, et al. Secreted protein acidic and rich in cysteine is a matrix scavenger chaperone. *PloS one*. 2011;6(9):e23880.
27. Alford JK, Rutt BK, Scholl TJ, Handler WB, Chronik BA. Delta relaxation enhanced MR: improving activation-specificity of molecular probes through R1 dispersion imaging. *Magnetic resonance in medicine : official journal of the Society of Magnetic Resonance in Medicine / Society of Magnetic Resonance in Medicine*. 2009;61(4):796-802.
28. Alford JK, Rutt BK, Scholl TJ, W.B H, Chronik BA. Delta relaxivity enhanced MR (dreMR): Theory of T1-slope weighted contrast *Proceedings of the ISMRM 16th Scientific Meeting*. Toronto, Canada 2008. Abstract 1443.
29. Koenig SH, Brown RD, 3rd, Adams D, Emerson D, Harrison CG. Magnetic field dependence of 1/T1 of protons in tissue. *Investigative radiology*. 1984;19(2):76-81.
30. Anordo E, Galli G, Ferrante G. Fast-field-cycling NMR: Applications and instrumentation. 2001(3):365-404.
31. Kimmich R, Anordo E. Field-cycling NMR relaxometry. *Progress in Nuclear Magnetic Resonance Spectroscopy*. 2004;44(3):257.
32. Koenig SH, Brown RD, Roy AK, Inglefield PT. *Field-cycling Relaxometry of Protein Solutions and Tissue: Implications for MRI*: Pergamon Press, 1990.
33. Lurie DJ, Aime S, Baroni S, et al. Fast field-cycling magnetic resonance imaging. *Comptes Rendus Physique*. 2010;11(2):136-48.
34. Rinck P, Fischer H, Vander Elst L, Van Haverbeke Y, Muller R. Field-cycling relaxometry: medical applications. *Radiology*. 1988;168(3):843-9.
35. Matter NI, Scott GC, Grafendorfer T, Macovski A, Conolly SM. Rapid polarizing field cycling in magnetic resonance imaging. *Medical Imaging, IEEE Transactions on*. 2006;25(1):84-93.
36. Mondino F, Filippi P, Magliola U, Duca S. Magnetic resonance relaxometry in Parkinson's disease. *Neurological Sciences*. 2002;23:87-8.
37. Lundbom N, Brown RD, 3rd, Koenig SH, Lansen TA, Valsamis MP, Kasoff SS. Magnetic field dependence of 1/T1 of human brain tumors. Correlations with histology. *Investigative radiology*. 1990;25(11):1197-205.
38. Kasoff SS, Spiller M, Valsamis MP, et al. Relaxometry of Noncalcified Human Meningiomas Correlation with Histology and Solids Content. *Investigative radiology*. 1995;30(1):49.
39. Pine KJ, Davies GR, Lurie DJ. Field-cycling NMR relaxometry with spatial selection. *Magnetic Resonance in Medicine*. 2010;63(6):1698-702.
40. Chen E-L, Kim RJ. Magnetic Resonance Water Proton Relaxation in Protein Solutions and Tissue: T₁ Dispersion Characterization. *PloS one*. 2010;5(1):e8565.
41. Hogain DC, Davies GR, Baroni S, Aime S, Lurie DJ. The use of contrast agents with fast field-cycling magnetic resonance imaging. *Physics in medicine and biology*. 2010;56(1):105.

42. Margaret Cheng H-L, Stikov N, Ghugre NR, Wright GA. Practical medical applications of quantitative MR relaxometry. *Journal of Magnetic Resonance Imaging*. 2012;36(4):805-24.
43. Ungersma SE, Matter NI, Hardy JW, et al. Magnetic resonance imaging with T1 dispersion contrast. *Magnetic Resonance in Medicine*. 2006;55(6):1362-71.
44. Alford JK, Scholl TJ, Handler WB, Chronik BA. An optimized insert coil for high-performance delta relaxation enhanced MR imaging of the mouse. *Proceedings of the ISMRM 18th Scientific Meeting*. Stockholm, Sweden 2010. Abstract 1551.
45. Harris CT, Handler WB, Dalrymple B, et al. Improvements in magnetic shielding of a B0 insert coil. *Proceedings of the ISMRM 20th Scientific Meeting*. Melbourne, Australia 2012. Abstract 2747.
46. Alford JK, Scholl TJ, Handler WB, Chronik BA. Design and construction of a prototype high-power B0 insert coil for field-cycled imaging in superconducting MRI systems. *Concepts in Magnetic Resonance Part B: Magnetic Resonance Engineering*. 2009;35B:1-10.
47. Alford JK, Scholl TJ, Handler WB, Rutt BK, Chronik BA. From static to dynamic: Construction of a B0 insert for field-cycled contrast in a clinical MR scanner *Proceedings of the ISMRM 20th Scientific Meeting*. Toronto, Canada 2008. Abstract 1171.
48. Bottomley PA, Foster TH, Argersinger RE, Pfeifer LM. A review of normal tissue hydrogen NMR relaxation times and relaxation mechanisms from 1-100 MHz: dependence on tissue type, NMR frequency, temperature, species, excision, and age. *Medical physics*. 1984;11(4):425-48.
49. Alford JK, Chronik BA. Quantification of bound contrast agent concentration using delta relaxation enhanced MR. *Proceedings of the ISMRM 18th Scientific Meeting*. Stockholm, Sweden 2010. Abstract 4937.
50. Mallett CL, McFadden C, Chen Y, Foster PJ. Migration of iron-labeled KHYG-1 natural killer cells to subcutaneous tumors in nude mice, as detected by magnetic resonance imaging. *Cytotherapy*. 2012;14(6):743-51.
51. Bernstein MA, King KF, Zhou ZJ. *Handbook of MRI pulse sequences*. Amsterdam ; Boston: Academic Press, 2004.
52. Parmelee DJ, Walovitch RC, Ouellet HS, Lauffer RB. Preclinical evaluation of the pharmacokinetics, biodistribution, and elimination of MS-325, a blood pool agent for magnetic resonance imaging. *Investigative radiology*. 1997;32(12):741-7.
53. Herborn CU, Waldschuetz R, Lauenstein TC, et al. Contrast-enhanced magnetic resonance imaging (MS-325) in a murine model of systemic lupus erythematosus. *Investigative radiology*. 2002;37(8):464-9.
54. Adzamli K, Yablonskiy DA, Chicoine MR, et al. Albumin-binding MR blood pool agents as MRI contrast agents in an intracranial mouse glioma model. *Magnetic resonance in medicine : official journal of the Society of Magnetic Resonance in Medicine / Society of Magnetic Resonance in Medicine*. 2003;49(3):586-90.
55. Folkman J. Role of angiogenesis in tumor growth and metastasis. *Seminars in oncology*. 2002;29(6 Suppl 16):15-8.
56. Preda A, van Vliet M, Krestin GP, Brasch RC, van Dijke CF. Magnetic resonance macromolecular agents for monitoring tumor microvessels and angiogenesis inhibition. *Investigative radiology*. 2006;41(3):325-31.
57. Brasch RC, Li KC, Husband JE, et al. In vivo monitoring of tumor angiogenesis with MR imaging. *Academic radiology*. 2000;7(10):812-23.
58. Brasch R, Turetschek K. MRI characterization of tumors and grading angiogenesis using macromolecular contrast media: status report. *European journal of radiology*. 2000;34(3):148-

59. Daldrup-Link HE, Okuhata Y, Wolfe A, et al. Decrease in tumor apparent permeability-surface area product to a MRI macromolecular contrast medium following angiogenesis inhibition with correlations to cytotoxic drug accumulation. *Microcirculation*. 2004;11(5):387-96.
60. Barrett T, Kobayashi H, Brechbiel M, Choyke PL. Macromolecular MRI contrast agents for imaging tumor angiogenesis. *European journal of radiology*. 2006;60(3):353-66.
61. Vandoorne K, Addadi Y, Neeman M. Visualizing vascular permeability and lymphatic drainage using labeled serum albumin. *Angiogenesis*. 2010;13(2):75-85.
62. Ogan MD, Schmiedl U, Moseley ME, Grodd W, Paajanen H, Brasch RC. Albumin labeled with Gd-DTPA. An intravascular contrast-enhancing agent for magnetic resonance blood pool imaging: preparation and characterization. *Investigative radiology*. 1987;22(8):665-71.
63. Schmiedl U, Ogan MD, Moseley ME, Brasch RC. Comparison of the contrast-enhancing properties of albumin-(Gd-DTPA) and Gd-DTPA at 2.0 T: and experimental study in rats. *AJR American journal of roentgenology*. 1986;147(6):1263-70.
64. Dafni H, Israely T, Bhujwala ZM, Benjamin LE, Neeman M. Overexpression of vascular endothelial growth factor 165 drives peritumor interstitial convection and induces lymphatic drain: magnetic resonance imaging, confocal microscopy, and histological tracking of triple-labeled albumin. *Cancer research*. 2002;62(22):6731-9.
65. Dafni H, Landsman L, Schechter B, Kohen F, Neeman M. MRI and fluorescence microscopy of the acute vascular response to VEGF165: vasodilation, hyper-permeability and lymphatic uptake, followed by rapid inactivation of the growth factor. *NMR in biomedicine*. 2002;15(2):120-31.
66. Dafni H, Gilead A, Nevo N, Eilam R, Harmelin A, Neeman M. Modulation of the pharmacokinetics of macromolecular contrast material by avidin chase: MRI, optical, and inductively coupled plasma mass spectrometry tracking of triply labeled albumin. *Magnetic resonance in medicine : official journal of the Society of Magnetic Resonance in Medicine / Society of Magnetic Resonance in Medicine*. 2003;50(5):904-14.
67. Hoelscher UC, Jakob PM. Eddy current compensation for delta relaxation enhanced MR by dynamic reference phase modulation. *Magma*. 2013;26(2):249-59.
68. Hoelscher UC, Lothar S, Fidler F, Blaimer M, Jakob P. Quantification and localization of contrast agents using delta relaxation enhanced magnetic resonance at 1.5 T. *Magma*. 2012;25(3):223-31.

Appendix A - Permissions

04/11/2012

RightsLink Printable License

WOLTERS KLUWER HEALTH LICENSE TERMS AND CONDITIONS

Nov 04, 2012

This is a License Agreement between Jonathan Araya ("You") and Wolters Kluwer Health ("Wolters Kluwer Health") provided by Copyright Clearance Center ("CCC"). The license consists of your order details, the terms and conditions provided by Wolters Kluwer Health, and the payment terms and conditions.

All payments must be made in full to CCC. For payment instructions, please see information listed at the bottom of this form.

License Number	3021740294200
License date	Nov 04, 2012
Licensed content publisher	Wolters Kluwer Health
Licensed content publication	Investigative Radiology
Licensed content title	Magnetic%20Field%20Dependence%20of%20T1%20of%20Protons%20in%20Tissue
Licensed content author	S%20H%20KOENIG,%20R%20D%20BROWN,%20D%20ADAMS,%20et%20al
Licensed content date	Jan 1, 1984
Volume Number	19
Issue Number	2
Type of Use	Dissertation/Thesis
Requestor type	Individual Account
Title of your thesis / dissertation	Delta Relaxation Enhanced Magnetic Resonance - Development and Application of a Field Cycling Contrast Mechanism
Expected completion date	Nov 2012
Estimated size(pages)	100
Billing Type	Invoice
Billing address	

Customer reference info	None
Total	0.00 USD
Terms and Conditions	

Terms and Conditions

1. A credit line will be prominently placed and include: for books - the author(s), title of book, editor, copyright holder, year of publication; For journals - the author(s), title of article, title of journal, volume number, issue number and inclusive pages.
2. The requestor warrants that the material shall not be used in any manner which may be considered derogatory to the title, content, or authors of the material, or to Wolters Kluwer.
3. Permission is granted for a one time use only within 12 months from the date of this invoice. Rights herein do not apply to future reproductions, editions, revisions, or other derivative works. Once the 12-month term has expired, permission to renew must be submitted in writing.
4. Permission granted is non-exclusive, and is valid throughout the world in the English language and the languages specified in your original request.
5. Wolters Kluwer cannot supply the requestor with the original artwork or a "clean copy."
6. The requestor agrees to secure written permission from the author (for book material only).
7. Permission is valid if the borrowed material is original to a Wolters Kluwer imprint (Lippincott-Raven Publishers, Williams & Wilkins, Lea & Febiger, Hanwal, Igaku-Shoin, Rapid Science, Little Brown & Company, Harper & Row Medical, American Journal of Nursing Co, and Urban & Schwarzenberg - English Language).
8. If you opt not to use the material requested above, please notify RightsLink within 90 days of the original invoice date.
9. Please note that articles in the ahead-of-print stage of publication can be cited and the content may be re-used by including the date of access and the unique DOI number. Any final changes in manuscripts will be made at the time of print publication and will be reflected in the final electronic version of the issue.
Disclaimer: Articles appearing in the Published Ahead-of-Print section have been peer-reviewed and accepted for publication in the relevant journal and posted online before print publication. Articles appearing as publish ahead-of-print may contain statements, opinions, and information that have errors in facts, figures, or interpretation. Accordingly, Lippincott Williams & Wilkins, the editors and authors and their respective employees are not responsible or liable for the use of any such inaccurate or misleading data, opinion or information contained in the articles in this section.
10. Other Terms and Conditions:

v1.3

If you would like to pay for this license now, please remit this license along with your payment made payable to "COPYRIGHT CLEARANCE CENTER" otherwise you will be invoiced within 48 hours of the license date. Payment should be in the form of a check or money order referencing your account number and this invoice number RLNK500890038.

Once you receive your invoice for this order, you may pay your invoice by credit card. Please follow instructions provided at that time.

Make Payment To:
Copyright Clearance Center
Dept 001
P.O. Box 843006
Boston, MA 02284-3006

For suggestions or comments regarding this order, contact RightsLink Customer Support: customerscare@copyright.com or +1-877-622-5543 (toll free in the US) or +1-878-646-2777.

Gratis licenses (referencing \$0 in the Total field) are free. Please retain this printable license for your reference. No payment is required.

Appendix B – Animal Protocol

Dr. Timothy Scholl
Associate Scientist, Robarts Research Institute
Assistant Professor, Department of Medical Biophysics
Schulich School of Medicine and Dentistry
Western University

Begin forwarded message:

From:
Subject: eSirius Notification - New Protocol Modification Has Been APPROVED2011-085::1
Date: 8 August, 2012 4:34:05 PM EDT
To:



AUP Number: 2011-085
PI Name: Scholl, Timothy
AUP Title: Development of Metabolic Probes for Magnetic Resonance Imaging of Mouse Models of Cancer

Official Notification of AUS Approval: A MODIFICATION to Animal Use Protocol 2011-085 has been approved.

The holder of this Animal Use Protocol is responsible to ensure that all associated safety components (biosafety, radiation safety, general laboratory safety) comply with institutional safety standards and have received all necessary approvals. Please consult directly with your institutional safety officers.

Submitted by: NTM, Support
on behalf of the Animal Use Subcommittee

The University of Western Ontario
Animal Use Subcommittee / University Council on Animal Care
Health Sciences Centre, • London, Ontario • CANADA – N6A 5C1
PH: 519-661-2111 ext. 86768 • FL 519-661-2028
Email: auspc@uwo.ca • <http://www.uwo.ca/animal/website/>

Appendix C – Animal Protocol



March 31, 2010

This is the Original Approval for this protocol
A Full Protocol submission will be required in 2014

Dear Dr. Foster:

Your Animal Use Protocol form entitled:
MRI of Cancer Cell Metastasis to the Mouse Lymph Nodes
Funding Agency Ontario Cancer Research Institute - UWO ROLA #R4174A11; National Cancer Institute of Canada
- UWO ROLA #R4174A10

has been approved by the University Council on Animal Care. This approval is valid from **March 31, 2010 to March 31, 2011**. The protocol number for this project is **2010-210 which replace 2006-013 which has expired.**

1. This number must be indicated when ordering animals for this project.
2. Animals for other projects may not be ordered under this number.
3. If no number appears please contact this office when grant approval is received.
If the application for funding is not successful and you wish to proceed with the project, request that an internal scientific peer review be performed by the Animal Use Subcommittee office.
4. Purchases of animals other than through this system must be cleared through the ACVS office. Health certificates will be required.

ANIMALS APPROVED FOR 4 Years

Species	4 Year Total Numbers Estimated as Required	List All Strain(s)	Age / Weight
Mouse	168	120 NuNu Foxn1(088) mice and 48 CB-17 SCID	18-22g

REQUIREMENTS/COMMENTS

Please ensure that individual(s) performing procedures on live animals, as described in this protocol, are familiar with the contents of this document.

The holder of this Animal Use Protocol is responsible to ensure that all associated safety components (biosafety, radiation safety, general laboratory safety) comply with institutional safety standards and have received all necessary approvals. Please consult directly with your institutional safety officers.

c.c. Approval - P. Foster, W. Lagerwerf

The University of Western Ontario
Animal Use Subcommittee / University Council on Animal Care
Health Sciences Centre, • London, Ontario • CANADA – N6A 5C1
PH: 519-661-2111 ext. 86770 • FL 519-661-2028 • www.uwo.ca/animal

Appendix D – CURRICULUM VITAE

EDUCATION

- 2010 – Present M.Sc., Medical Biophysics**
Western University, London, ON, Canada
Collaborative Program in Molecular Imaging
- 2005 - 2010 Honours B.Sc., Medical Physics Co-Operative**
Ryerson University, Toronto, ON, Canada

HONOURS AND AWARDS

- 2011 - 2013** CIHR Strategic Training Program in Vascular Research
- 2010 - 2013** Western Graduate Research Scholarship
- 2012** Student Travel Stipend, *5th Annual World Molecular Imaging Congress*
- 2010** Top 4th year Thesis Presentation, *Ryerson University*
- 2008** Clyde Logue Memorial Award, *Ryerson University (Highest 3rd year GPA)*
- 2007** Ontario First Generation Award, *Ryerson University*
- 2006** Ryerson University Student Bursary Award
- 2006** Ryerson University Student Union Bursary Award
Dean's List (*2005/2006, 2006/2007, 2007/2008*)

RESEARCH EXPERIENCE

- Sep 09-Apr 10 Undergraduate Research Thesis, CT-Guided Robotic Lung Biopsy**
Ryerson University, Toronto, ON, Canada
- May 08-Sep 09 Undergraduate Research Assistant, Applied Modern Physics Group, P-21**
Superconducting Quantum Interference Device (SQUID) Team
Los Alamos National Laboratory (LANL), Los Alamos, New Mexico, USA
Supervisor: Michelle Espy, PhD

LEADERSHIP AND VOLUNTEER WORK

- Mar 07-May 08 Lead Facilitator, Visions of Science**
Ryerson University, Toronto, ON, Canada
- Sep 07 - Apr 08 Mentor, Tri-Mentoring Program**
Ryerson University, Toronto, ON, Canada

EXTRACURRICULAR ACTIVITIES

- Sep 07 - Apr 08 Vice-President Social Life and Events (Elected)**
Medical Physics Student Council, Ryerson University
- Sep 07 - Apr 08 Undergraduate Representative (Elected)**
- Sep 06 - Apr 07 Physics Departmental Council, Ryerson University**
- Sep 06 - Apr 07 Vice-President Finance (Elected)**
Medical Physics Student Council, Ryerson University

PUBLICATIONS AND PRESENTATIONS

Oral Presentations

- FM. Martinez, **Y. Araya**, CT. Harris, WB. Handler, BA. Chronik, T.J. Scholl, “Improving Contrast of Delta Relaxation Enhanced Magnetic Resonance (dreMR) Imaging”, 21st International Society for Magnetic Resonance in Medicine, Salt Lake City, Utah USA (April 2013). Abstract 0560.
- **Y. T. Araya**, F. M. Martinez, C. T. Harris, W. B. Handler, B. A. Chronik, T. J. Scholl, “Targeted-Albumin using dreMR in a Murine Prostate Cancer Model”, Annual Ontario Institute for Cancer Research Scientific Meeting, Toronto, Canada (March 2013).
- **Y. Araya**, FM. Martinez, CT. Harris, WB. Handler, BA. Chronik, TJ. Scholl, “Direct Albumin Imaging using a Delta Relaxation Enhanced Magnetic Resonance Double Inversion Recovery Fast Spin Echo Sequence”, 5th Annual World Molecular Imaging Congress, Dublin, Republic of Ireland (September 2012). Abstract SS1.

Poster Presentations

- FM. Martinez, **Y. Araya**, CT. Harris, WB. Handler, BA. Chronik, T.J. Scholl, “Improving Contrast of Delta Relaxation Enhanced Magnetic Resonance Imaging”, 11th Annual Imaging Network of Ontario Conference, Toronto, Canada (February 2013).
- **Y. Araya**, “Ct-Guided Robotic Lung Biopsy”, Annual 4th year Thesis Symposium, Ryerson University, Toronto, Canada (May 2010).
- **Y. Araya**, P. Nath, M. Espy, “A Permanent Magnet Circuit with Tunable Magnetic Gradients for Magnetophoresis”, 9th Annual Student Symposium, Los Alamos National Laboratory, New Mexico, USA (August 2009).
- **Y. Araya**, “Development of A Robust Chamber for High-Throughput Flow Based Magnetic Spectrometer”, 8th Annual Student Symposium, Los Alamos National Laboratory, New Mexico, USA (August 2008).